The Cryosphere

A long-term proxy for sea ice thickness in the Canadian Arctic: 1996–2020

Isolde A. Glissenaar[1], **Jack C. Landy**[2], **David G. Babb**[3], **Geoffrey J. Dawson**[1], and **Stephen E. L. Howell**[4]

[1]Bristol Glaciology Centre, School of Geographical Sciences, University of Bristol, Bristol, UK
[2]Centre for Integrated Remote Sensing and Forecasting for Arctic Operations, Department of Physics and Technology, UiT The Arctic University of Norway, Tromsø, Norway
[3]Centre for Earth Observation Science, University of Manitoba, Winnipeg, MB, Canada
[4]Climate Research Division, Environment and Climate Change Canada, Toronto, ON, Canada

Correspondence: Isolde A. Glissenaar (isolde.glissenaar@bristol.ac.uk)

Abstract. This study presents a long-term winter sea ice thickness proxy product for the Canadian Arctic based on a random forest regression model – applied to ice charts and scatterometer data, trained on CryoSat-2 observations, and applying an ice type–sea ice thickness correction using the Pan-Arctic Ice Ocean Modeling and Assimilation System (PIOMAS) – that provides 25 years of sea ice thickness in the Beaufort Sea, Baffin Bay, and, for the first time, the Canadian Arctic Archipelago. An evaluation of the product with in situ sea ice thickness measurements shows that the presented sea ice thickness proxy product correctly estimates the magnitudes of the ice thickness and accurately captures spatial and temporal variability. The product estimates sea ice thickness within 30 to 50 cm uncertainty from the model. The sea ice thickness proxy product shows that sea ice is thinning over most of the Canadian Arctic, with a mean trend of -0.82 cm yr^{-1} in April over the whole study area (corresponding to 21 cm thinning over the 25-year record), but that trends vary locally. The Beaufort Sea and Baffin Bay show significant negative trends during all months, though with peaks in November (-2.8 cm yr^{-1}) and April (-1.5 cm yr^{-1}), respectively. The Parry Channel, which is part of the Northwest Passage and relevant for shipping, shows significant thinning in autumn. The sea ice thickness proxy product provides, for the first time, the opportunity to study long-term trends and variability in sea ice thickness in the Canadian Arctic, including the narrow channels in the Canadian Arctic Archipelago.

1 Introduction

Sea ice thickness (SIT) is a key variable when characterizing an ice cover and its impact on the local environment and provides important insight into how an ice cover changes in response to climate change. Unfortunately, observations of ice thickness at appropriate spatial and temporal scales are sparse. Seasonal estimates of ice thickness from satellite altimeters only go back to 2003, while year-round observations only extend back to 2010 (Landy et al., 2022) and represent a rather short record for examination of long-term trends and variability. In place of observations, reanalyses such as the Pan-Arctic Ice Ocean Modeling and Assimilation System (PIOMAS, Zhang and Rothrock, 2003) are commonly used to provide long-term estimates of ice thickness. However, PIOMAS is known to overestimate thinner ice and underestimate thicker ice (Schweiger et al., 2011). Furthermore, both satellite altimeters and PIOMAS have difficulty resolving ice thickness in coastal areas and either mask out or have a high degree of uncertainty over the Canadian Arctic Archipelago (CAA). Satellite altimeters are limited in their application within the CAA because of a combination of a lack of leads within the seasonally landfast ice cover, strong tidal cycles, and a lack of snow depth products, which collectively result in large uncertainties in sea ice freeboard (Ricker et al., 2014). PIOMAS has a high degree of uncertainty within the CAA due to a mixture of seasonal and multi-year sea ice (Howell et al., 2016). As a result, observations of ice thickness within the CAA are confined to a few opportunistic observations (i.e. Melling, 2002; Haas and Howell,

2015; Melling et al., 2015). Despite the difficulty in observing ice thickness within the CAA, it is estimated to contain about 10 % of the Northern Hemisphere sea ice volume (Lietaer et al., 2008) and is home to some of the oldest and thickest multi-year ice (MYI) in the Arctic (Bourke and Garrett, 1987; Barber et al., 2018; Haas et al., 2010; Melling, 2022). The CAA is an important pathway bringing cold, fresh Arctic water to the Labrador Sea (Melling et al., 2008), which is an important site for deep convection and plays a key role in the large-scale meridional overturning circulation (e.g. Marshall and Schott, 1999). Moreover, the CAA is bisected by the Northwest Passage and is home to many northern communities that rely on maritime traffic for resupply (Dawson et al., 2020). As the ice cover declines, ship traffic across the Canadian Arctic has dramatically increased since the 1990s (Pizzolato et al., 2014), and sea ice poses the greatest risk to ships operating within the CAA. Understanding the changes in ice thickness within the CAA and monitoring it in the future is therefore of vital importance.

Here, we combine information from the Canadian Ice Service (CIS) ice charts and aggregated scatterometer backscatter data to create a proxy SIT product over the Canadian Arctic, including the Beaufort Sea, Baffin Bay, and the CAA (Fig. 1), for November–April from 1996 to 2020. We apply machine-learning methods to these long-term remote-sensing datasets and CryoSat-2 SIT observations to determine the relationship between sea ice stage of development, form of ice, backscatter, and SIT to create the SIT proxy product. Additionally, this machine-learning model can be used moving forward to provide estimates of ice thickness whenever ice charts and scatterometer imagery are available. Within the paper Sect. 2 introduces the datasets and Sect. 3 the applied methods. Section 4 evaluates the proxy product versus satellite and in situ observations of SIT. Section 5 presents the results of the proxy product and discusses the emergent trends and variability of SIT in the Canadian Arctic.

2 Data

2.1 Canadian Ice Service ice charts

The CIS has produced ice charts for the Canadian Arctic (Fig. 1) since the 1960s that include information on sea ice concentration, stage of development (relating to age and ranging from new ice to multi-year ice), and form of ice (relating to floe size or kind of ice, e.g. icebergs or fast ice) using the World Meteorological Organization egg code. The ice charts use polygons to represent different ice regimes, consisting of up to three different stages of development and forms of ice. The uncertainty in the ice charts has been reviewed, and the data were validated for use in climate studies (see the Canadian Ice Service (CIS), 2007a; Tivy et al., 2011). Numerous studies have used the ice charts to study

trends and variability in sea ice cover (Tivy et al., 2011; Mudryk et al., 2018; Derksen et al., 2018), to quantify loss of multi-year ice in the Canadian Arctic (Galley et al., 2016; Babb et al., 2022; Howell et al., 2022), and to research causes of sea ice extremes (Howell et al., 2010; Babb et al., 2019, 2020). The ice charts are produced by ice analysts who compile available aerial, shipping, and remote-sensing data, though since 1996 RADARSAT has been the primary data source (Canadian Ice Service (CIS), 2007b; Tivy et al., 2011).

Previous studies have shown that there is a direct relationship between ice age and SIT and have used this relationship to propose simple linear models that derive SIT for March (Maslanik et al., 2017; Tschudi et al., 2016; Liu et al., 2020). Additionally, floe size has been shown to be related to ice age and ice thickness as thicker MYI floes tend to be larger than FYI floes (Tilling et al., 2019; Hwang et al., 2017; Aldenhoff et al., 2019). The variables stage of development (from here on called ice type) and form of ice in the CIS ice charts are related to observed SIT (Fig. 2), which gives the possibility of using the ice charts to estimate ice thickness. The stages of development used in the ice charts are provided with an estimated range of SIT. However, the actual relations between the stages of development, form of ice, and SIT are currently unknown.

The weekly regional ice charts have all been digitized and are freely available at https://iceweb1.cis.ec.gc.ca/ (last access: 1 March 2023). This study uses the ice charts for the Western Arctic and Eastern Arctic for November–April 1996–2020, since the start of the ice analyses using RADARSAT as the primary data source (Fig. 1). The temporal availability of the ice charts varies from monthly to weekly (see Supplement Table S1) and changes in spatial coverage slightly in 1997 and 1998.

2.2 Scatterometer data

Within the CIS chart polygons, the mixture of stages of development and forms of ice is assumed to be uniform, whereas we expect sea ice to be more spatially variable on a smaller scale. Because of this, the dataset was supplemented with scatterometer image reconstruction (SIR) sigma-naught-calibrated backscatter data (Early and Long, 2001) from multiple scatterometer satellites. Scatterometer backscatter records, going back to 1992, were previously used to create ice age products (e.g. Zhang et al., 2019; Lindell and Long, 2016) and are suggested by Belmone Rivas et al. (2018) as a reliable proxy in the historical reconstruction of SIT due to their spatial correlation with observed ice thicknesses. As there is no continuous record of one instrument over the entire 1996–2020 record, we use data from multiple satellite scatterometers that operate in the C band (4–8 GHz) and Ku band (12–18 GHz) (Fig. 3). Each of the scatterometers used in this study is detailed in Appendix A.
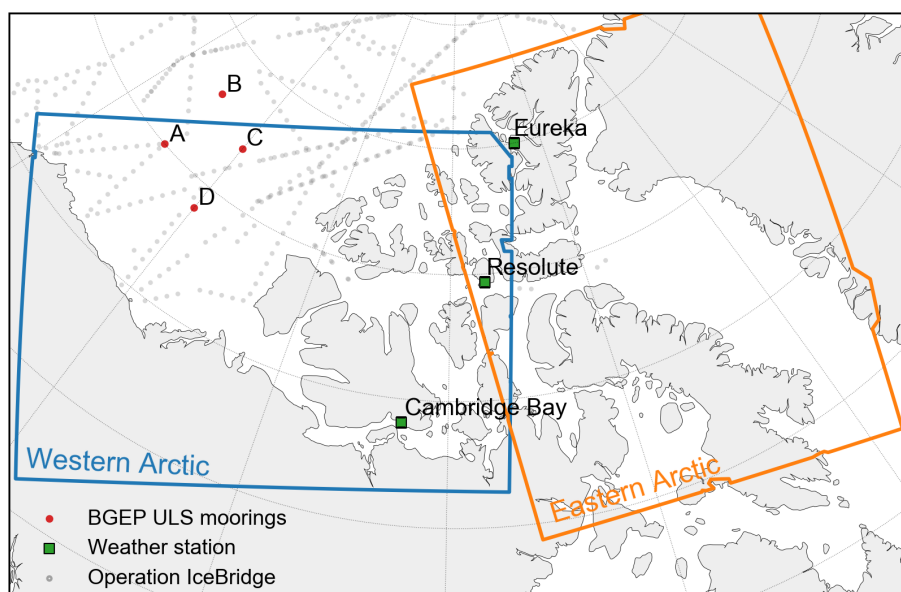
Figure 1. Overview of the study area with locations of the Canadian Ice Service regional ice charts for the Western Arctic and Eastern Arctic (Canadian Ice Service (CIS), 2007a), the BGEP ULS moorings (Krishfield and Proshutinsky, 2006), the weather stations for measuring landfast ice thickness (Brown and Cote, 1992), and Operation IceBridge flight paths (Kurtz et al., 2015).
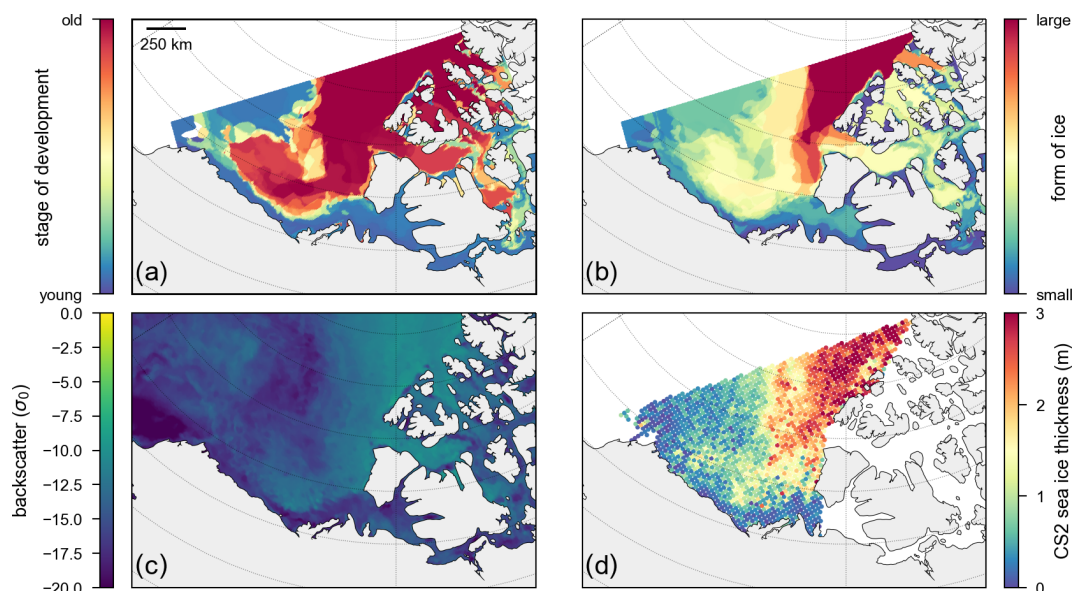

Figure 2. One snapshot of the remote-sensing input data compared to observed sea ice thickness in November 2018 with the **(a)** stage of development from the CIS ice charts, **(b)** form of ice from the CIS ice charts, **(c)** scatterometer backscatter from ASCAT, and **(d)** CryoSat-2-observed sea ice thickness.

After comparing the different scatterometer data products, we determined that there was no bias between the different sensors operating in the same band and combined the datasets into a long-term record for each wavelength. As the wavelengths interact differently with snow and ice (Ontstott, 1992), we expect C-band and Ku-band instruments to give different results and do not combine scatterometer data from

the different bands into one record. C-band scatterometer data from European Remote Sensing Satellite (ERS)-1, ERS-2, and the Advanced Scatterometer (ASCAT) were combined into one record from 1996 to 2020 with a gap from 2001 to 2007. Ku-band scatterometer data from the Quick Scatterometer (QuikSCAT), OSCAT-1, and OSCAT-2 were combined into one record from 1999 to 2020 with a gap from 2014 to

Table 1. Details of the scatterometer data.

	Time period	Frequency	Launched by
ERS-1[1]	January 1996–April 1996	C-band	ESA
ERS-2[1]	November 1996–January 2001	C-band	ESA
ASCAT[1]	January 2007–December 2020	C-band	ESA
QuikSCAT[1]	November 1999–November 2009	Ku-band	NASA
OSCAT-1[1]	November 2009–February 2014	Ku-band	ISRO
OSCAT-2[2]	November 2016–December 2020	Ku-band	ISRO

[1] Obtained from the NASA Scatterometer Climate Record Pathfinder (SCP): https://www.scp.byu.edu/data/ (last access: 1 June 2023). [2] Obtained from MOSDAC: https://mosdac.gov.in/satellite-catalog (last access: 10 February 2022).

2017. More details on the satellites, an analysis of the data, and a justification for using the long-term time series without bias correction are provided in Appendix A.

2.3 CryoSat-2

We used seasonal ice thickness measurements derived from the ESA's CryoSat-2 radar altimeter for November to April for the period 2010 to 2020 using the methodology described in Landy et al. (2020). This methodology applies a numerical model for a backscattered CryoSat-2 synthetic aperture radar (SAR) echo waveform to retrieve sea ice freeboard, assuming log-normal statistics for the sea ice height and roughness distribution, and the SnowModel-LG snow depth and density (Liston et al., 2020) to estimate SIT. We use monthly SIT observations on a 50 km grid. However, we mask out SIT observations from the Canadian Arctic Archipelago (as defined by MASIE-NH regions, Fetterer et al., 2010), as we cannot reliably obtain SIT measurements with land contamination of the return echo, a lack of leads reduces the performance of CryoSat-2, and the SnowModel-LG product is not available in this region. We also removed outliers in the data by excluding any SIT measurement with an uncertainty in the top-5th percentile (more than 0.48 m).

3 Methods

3.1 Creating a training dataset

We trained the machine-learning model using a dataset from November–April 2010–2020 of predictor features including the partial concentration (between 0 and 1) of each ice type (new ice, nilas, multi-year ice, etc.) and form of ice (pancake, small ice cake, giant floe, etc.) from the ice charts and scatterometer data. This resulted in 24 input variables (see Supplement Table S2 for a full list of the used predictor features). These data were gridded to the same 50 km resolution as the CryoSat-2 SIT observations, which are used as coincident
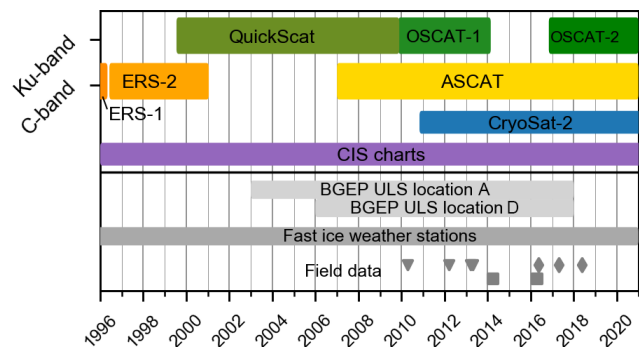

Figure 3. Timeline of the availability of used data in the machine-learning model and in situ data used for validation. Field data triangles refer to Operation IceBridge campaigns, squares to the ECCC fast ice measurements in Eureka, and diamonds to the fast ice measurements in Cambridge Bay.

reference observations on which to train the model. Sea ice drift moving ice between grid cells during the month might introduce some uncertainty, especially in the Beaufort Gyre, where the drift is high (Petty et al., 2016). However, with the low resolution of 50 km of the dataset, we assume that this effect will not be large. As the CryoSat-2 SIT observations have been masked out for the Canadian Arctic Archipelago, this region is not included in the training dataset. Nevertheless, the distribution of the features in the training region was after inspection determined to be representative of the full region. Each grid node was taken as an individual data point to be used in the training. Separate training datasets were created for the C-band and Ku-band scatterometer data. As the relationship between ice age and SIT varies over time in the sea ice growth season, the training dataset was separated by month. The number of points in the training datasets varies from 14 642 to 30 601 (full list in Supplement Table S2).

The categories second-year ice (SYI) and MYI were not used in the ice charts for the months of January–April during the training period (2010–2020) but have been used in the

ice charts for previous years of the long-term record; therefore, we could not use these variables. Instead, we combined the SYI and MYI features for January–April into the overarching "old ice" feature, which appears consistently in the training period and the full record. There are some other rare instances where a feature is used in the long record of predicting features but not in the training dataset. These other features do not have overarching categories, so we decided to remove the sporadic instances where this feature has a partial concentration of more than 50 % within a grid cell.

3.2 Random forest regression model

After comparing the performances of linear regression, decision tree regression, and gradient-boosting regression, a random forest regression model was selected as the most suitable machine-learning model for this task. We trained the random forest regression model to find the relation between the predictor features (the ice type, form of ice, and backscatter) and observations (CryoSat-2-observed SIT) in order to create a proxy SIT record for 1996–2020. The full processing chain is visualized in Fig. 4. Random forest regression is a supervised learning algorithm that uses ensemble learning. A random forest operates by constructing several decision trees during training and outputting the final predicted value as the mean prediction of all the trees. A random forest is a powerful model capable of finding complex non-linear relationships in data.

The optimal parameters were selected using the Python package scikit-learn's hyperparameter tuning function GridSearchCV. The number of trees in the forest was set at 95, the maximum depth of the separate trees is 15 levels, and the number of features to consider when looking for the best split was set at 5. The other hyperparameters were set at their default values. A separate random forest regression model was created for each month in November–April. There are also separate models for the datasets with Ku-band scatterometer data and C-band scatterometer data. The results of these were combined after the SIT prediction was made by taking the mean of the two results when both are available (Fig. 3).

The results for December 1996–April 1997 were removed from the analysis of the proxy SIT product as they showed unreasonably high SIT results (> 1 m thicker than in other years) caused by the Canadian ice charts showing a full cover of old ice in the Beaufort Sea. This was deemed highly unlikely, as such a large area appeared very differently, for these months, in all the other years of the ice chart record. ERS-2 scatterometer backscatter supports the higher MYI concentration in the southern Beaufort Sea in this year, showing higher backscatter. However, ERS-2 scatterometer backscatter does not support these extreme conditions in the entire Beaufort Sea in the ice charts as there is no anomaly in ERS-2 scatterometer data in the western Beaufort Sea and the central Arctic. We assume it was an overestimation in the interpretation by the ice analyst.

3.3 Correction to thinning of ice types

One of the assumptions in the generated SIT proxy product is that the relation between the inputs (ice type, form of ice, and scatterometer backscatter) and the SIT stays consistent during the period when the model is applied (1996–2020). However, we know that over the recent past Arctic multi-year ice has thinned (Kacimi and Kwok, 2022; Krishfield et al., 2014). In order to correct for this change, we retrieved the linear least-squares trend in PIOMAS mean thickness (available at http://psc.apl.uw.edu/research/projects/arctic-sea-ice-volume-anomaly/data/model_grid, last access: 2 February 2022) of the three coincident overarching categories (multi-year ice, first-year ice (FYI), and young ice) for the region covered by the ice charts and for the period 1996–2020. The region of PIOMAS data within the Canadian Arctic channels was masked out. Trends are presented in Table 2: there are significant ($p < 0.1$) negative trends for MYI for every month between November and March and for FYI for every month except November and March. For the categories and months where the trend is significant, the trend was applied as a correction to the SIT results in the proxy product as follows:

$$\mathrm{SIT_{corr}} = \mathrm{SIT} + t$$
$$\cdot \, (\mathrm{trend_{MYI}} \cdot C_{\mathrm{MYI}} + \mathrm{trend_{FYI}} \cdot C_{\mathrm{FYI}} + \mathrm{trend_{YI}} \cdot C_{\mathrm{YI}}), \quad (1)$$

where SIT is the sea ice thickness, trend is the sea ice thickness trend over time within the given ice category, t is the time in years prior to 2015 (the middle of the training data period), and C is the partial concentration of the given ice category. We present both the raw SIT from the proxy product, which we refer to as proxy_nocorr, and a product corrected for changes in SIT within specific categories, which we refer to as proxy_corr. The proxy_nocorr SIT product quantifies the sea ice thickness change due to changes in ice type, floe size, and scatterometer backscatter and can be used to study sea ice thickness variability and to be applied to newly released ice charts. The proxy_corr product can be used when determining long-term trends in SIT, accounting for changes due to ice type, floe size, and backscatter as well as expected changes in the relationship between SIT and ice type. There are significant uncertainties associated with PIOMAS sea ice thickness observations (Schweiger et al., 2011), and we can expect these to be highest within the channels of the Canadian Arctic. Numerical simulation of the sea ice dynamics and ice–ocean exchanges is challenging within such a complex fjord environment, and the PIOMAS solution is constrained by satellite data such as passive-microwave sea ice concentrations that are also uncertain in this region. For this reason, we mask out the CAA channels when estimating long-term SIT trends by ice type and consider the proxy_corr SIT product to be more accurate for analysing trends within the Canadian Arctic channels than simply using the PIOMAS data.
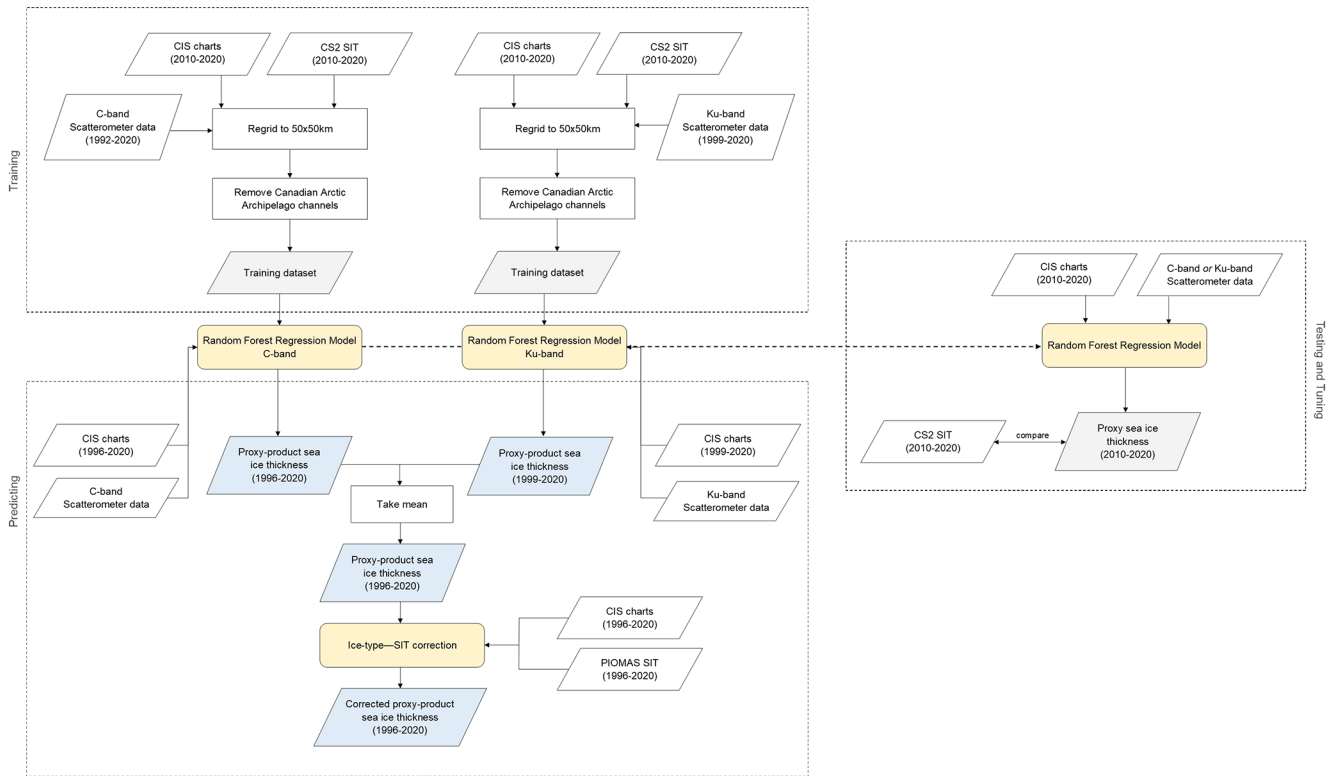
Figure 4. Schematic of the applied data and methods to create the sea ice thickness proxy product.

Table 2. PIOMAS trends in sea ice thickness in the main ice type categories ($cm\,yr^{-1}$). No number is given when this is not significant ($p > 0.1$).

	Young ice	First-year ice	Multi-year ice
November	–	–	−3.0
December	–	−0.9	−3.8
January	–	−0.4	−2.8
February	–	−0.6	−1.8
March	–	−0.5	−1.5
April	–	−0.6	–

3.4 Comparison with independent SIT datasets

The proxy SIT product, both before and after application of the ice type–SIT correction, was compared with independent in situ and airborne SIT measurements.

3.4.1 Upward-looking sonar (ULS) moorings

The Beaufort Gyre Exploration Project (BGEP) investigates basin-scale mechanisms in the Beaufort Gyre. As part of this project, the sea ice draft is measured at four locations in the Beaufort Gyre using moored ULS instruments (https:

//www2.whoi.edu/site/beaufortgyre/data/mooring-data/, last access: 7 June 2022, Krishfield and Proshutinsky, 2006). Three of these locations fall within the area of the ice charts, though only data from moorings A and D (74°59′ N, 149°58′ W and 73°59′ N, 139°59′ W, respectively; see Fig. 1) are considered as they provide a long continuous daily record of ice draft (2003–2020 for location A and 2006–2020 for location D). The sea ice draft was converted to SIT assuming hydrostatic equilibrium: $h_i = \frac{\rho_w}{\rho_i} h_d - \frac{\rho_s}{\rho_i} h_s$. h_i is sea ice thickness; h_d is sea ice draft; h_s is snow depth; and ρ_w, ρ_i, and ρ_s are the densities of seawater, sea ice, and snow, respectively. Snow depth and density were retrieved from the Lagrangian snow evolution model SnowModel-LG (Liston et al., 2020; Stroeve et al., 2020), i.e. the same snow dataset used in the CryoSat-2 SIT product. The seawater density was assumed to be $1024\,kg\,m^{-3}$. Sea ice density was assumed to be $916.7\,kg\,m^{-3}$ for FYI and $882\,kg\,m^{-3}$ for MYI (Alexandrov et al., 2010). The observed ULS SIT was averaged monthly and compared to the closest 10 grid cells in the SIT proxy product.

3.4.2 Operation IceBridge

NASA's Operation IceBridge (OIB) provides airborne retrievals of sea ice thickness during spring using a combination of laser and radar altimeter sensors. Campaigns in April 2009, April 2010, March 2011, March 2012, March

2013, and April 2013 included flights over sea ice in the western Canadian Arctic. SIT from the OIB L4 Sea Ice Freeboard, Snow Depth, and Thickness (IDCSI4) product (https://nsidc.org/data/idcsi4/versions/1, Kurtz et al., 2015) for these six campaigns was used. Measurements with an uncertainty higher than 1 m were removed. The spatial resolution of this product is 40 m. As we aim to compare the OIB SIT data to the SIT proxy product, we average every 1250 measurements to create a product with a spatial resolution of 50 km. When less than half of the measurements over the averaging window have no value, the sample is removed.

3.4.3　In situ measurements

The Canadian Ice Thickness Program has collected ice thickness and snow depth measurements on landfast ice near weather stations as far back as 1947 (https://www.canada.ca/en/environment-climate-change/ services/ice-forecasts-observations/latest-conditions/ archive-overview/thickness-data.html, last access: 9 August 2022). Measurements are taken at approximately the same location every year on a weekly basis, starting after freeze-up when the ice is safe to walk on and continuing until break-up or when the ice becomes unsafe. The data have been summarized by Brown and Cote (1992) and Howell et al. (2016). Ice thickness is measured using an auger kit or a hot-wire ice thickness gauge. Three of the sites are located within the study area: Cambridge Bay, Resolute, and Eureka (see Fig. 1). This allows for validation of the SIT proxy product in the CAA channels. We compared the fast ice thickness measurements to the closest 10 grid cells in the SIT proxy product.

Additional observations of landfast ice thickness were collected near Eureka in March and April 2014 and April 2016 by Environment and Climate Change Canada (ECCC) (King et al., 2015, 2020) and near Cambridge Bay in May 2016, April 2017, and May 2018. Observations were collected using manual ice augers and are used for further comparison to the closest 10 grid cells in the SIT proxy product.

4　Model performance

4.1　Model evaluation

We evaluated the model performance by first calculating the testing and training errors for each of the models (each month and using both the Ku-band and C-band scatterometer datasets) (Fig. 5). The training error was determined from the root-mean-square error (RMSE) by testing on the same data as the model was trained on. The training error tells us how well the model captures the relation between predictor features and observations of the data it was trained on. The testing error was calculated using a 10-fold cross-validation RMSE of the validation dataset, which is determined by splitting the randomly shuffled dataset into 10 groups and for
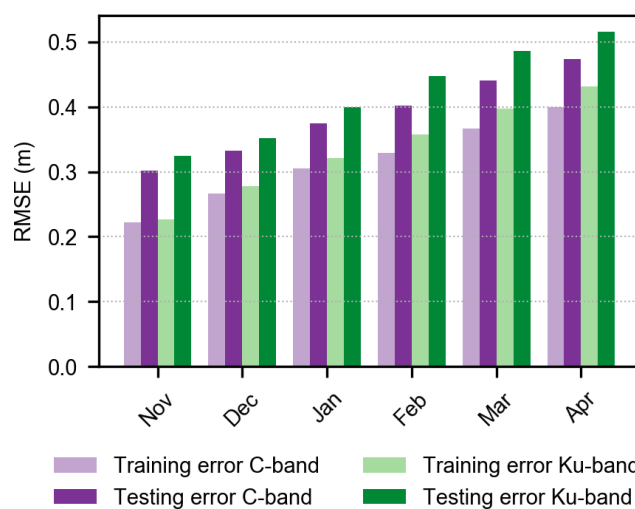

Figure 5. Training and testing errors in the random forest regression models for each month and scatterometer frequency (C-band and Ku-band).

each unique group holding that group out as test data, training the model on the other 9 groups, and determining the RMSE in the test group. This is done for each of the 10 groups, and then the mean of the RMSEs is taken as the testing error. The testing RMSE varies between 30 and 50 cm, depending on the month and scatterometer dataset, with the RMSE error being greater for months later in the growth season (Fig. 5). The testing error is expectedly larger than the training error for each of the models. However, the difference is small (~ 0.05 m), which suggests that the model is not over-fitted (Géron, 2019). The error is larger for the Ku-band dataset than for the C-band dataset, likely because there are more training data available with the C-band dataset as the C-band scatterometers cover the entire training period (2010–2020), whereas there is no Ku-band scatterometer available for the period 2014–2017 (see Table S3 for the number of training instances), and there is a difference in interaction with snow and ice from the different scatterometer wavelengths (Ontstott, 1992).

We also evaluated the model by not using a randomly selected 20 % of the original CryoSat-2 dataset for the training and reserving it for a validation dataset. This allowed us to plot the predicted versus observed SIT from the validation dataset (Fig. 6). The trend line fits closely over the 1 : 1 line, showing that there is no clear overestimation or underestimation of the ice thickness at thin or thick ends of the scale, and the random forest regression captures the non-linear relationships between the input features and SIT. However, there are outliers where the prediction is more than 1 m larger or smaller than the observed SIT. This is likely the result of the main input data from the ice charts being polygons with homogenized fields covering large areas, so the random forest
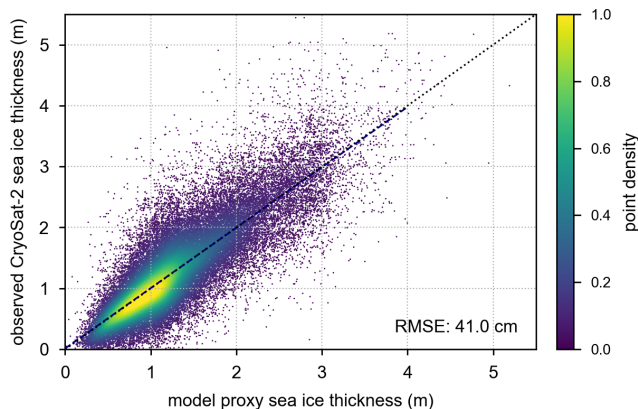
Figure 6. Model performance when the proxy product is compared with CryoSat-2-observed sea ice thickness not included in the model training step. The dashed line shows the trend line closely following the dotted 1 : 1 line. Colours refer to the point density.

regression model is incapable of predicting these small-scale local variations in thickness observed by CryoSat-2.

Finally, to analyse the model performance spatially and to evaluate the model's capability to capture yearly variability, the model was trained on a dataset including all years of the CryoSat-2 record, except for the 2017–2018 winter, and used to predict the SIT for this winter (Fig. 7). The predicted SIT for November 2017 very closely resembles the observed SIT. The error in the prediction is larger for April 2018, although the patterns in SIT are generally predicted correctly. There is an area of the Beaufort Sea where the ice thickness is overestimated by the model and an area along the coast of Alaska where the ice thickness is underestimated compared to CryoSat-2. In these cases, the variations in CryoSat-2 SIT were not reflected by similar patterns in the ice charts or scatterometer data, and they likely reflect dynamic deformation of the ice pack that underlies the ice type.

4.2 Comparison with independent SIT datasets

For an independent validation of the model, we compared the SIT proxy product with in situ and aerial observations. Typically, the validation statistics were improved with the application of the ice type–SIT correction, so we therefore use the proxy_corr SIT product for subsequent analyses.

4.2.1 ULS moorings

A comparison between the SIT proxy product and SIT at the BGEP ULS moorings in November and April at moorings A and D is shown in Fig. 8. The mooring data allowed us to investigate the temporal performance of the proxy SIT product in the Beaufort Sea. The SIT proxy product shows similar magnitude and yearly variability to the ULS measurements. At location A, the proxy product and the ULS SIT have a correlation coefficient of 0.77 and an RMSE of 0.35 m, and

for location D there is a correlation coefficient of 0.74 and an RMSE of 0.35 m. The RMSE is within the range of the model testing uncertainty (30–50 cm) (Fig. 5), showing that the proxy product predicts SIT at this location well. Since the model testing uncertainty is only based on its performance against CryoSat-2 SIT observations, which have their own uncertainties, it is encouraging that there is a similar RMSE when comparing the SIT proxy product to independent ULS observations.

We determined the anomaly correlation coefficient (ACC) to be 0.45 and 0.49 at locations A and D, respectively, after removing the climatological seasonal cycle from both datasets. The ACCs are improved by 26 % on average when using the proxy_corr rather than proxy_nocorr SIT product. These positive ACCs show that the yearly variability between the proxy product and the ULS SIT is comparable and typically going in the same direction. The model is thus capable of determining an anomalously high- or low-SIT year at these two locations; however, the magnitudes of the ice thickness anomalies can be up to 0.5 to 1 m different. As an example, the proxy product correctly estimates the high SIT in November 2013 and the low SIT in November 2016 at both mooring locations in the Beaufort Gyre (Fig. 7). The proxy product correctly estimates the SIT in November 2012 to be below average at mooring D (at 0.78 m) but does not get the magnitude of the SIT minimum right (0.34 m according to the mooring), and it does not estimate November 2012 to be below average at mooring A. However, the proxy product does estimate SIT very close to the observed CryoSat-2 SIT at the location of the ULS BGEP moorings for November, and as the model is trained on CryoSat-2 data, it is not expected to do better than CryoSat-2. Moreover, the mean seasonal cycle is captured very well, with a mean difference between the proxy SIT and the ULS mooring of only 1 cm in November and 14 cm in April (see Fig. S2 in the Supplement).

4.2.2 Operation IceBridge

The results of the comparison of the SIT proxy product with overlapping Operation IceBridge tracks gives us insight into how well the proxy product captures regional variability in the Beaufort Sea. The proxy product generally captures the spatial patterns and magnitudes of SIT as observed by OIB campaigns during the end of winter (Fig. 9). The SIT proxy product correctly captures the spatial pattern of thicker sea ice in the north-eastern Beaufort Sea and thinner sea ice to the south.

The proxy product is found to underestimate ice thickness along the western coast of the CAA, north of the Queen Elizabeth Islands, in April 2010 and along the northern coast of Alaska near Point Barrow in March 2012. Both these months are characterized by high RMSEs when comparing OIB with the proxy SIT product (1.13 m in April 2010 and 0.83 m in March 2012). In April 2010 the input data in the model are characterized by smaller floe sizes in the ice chart than other
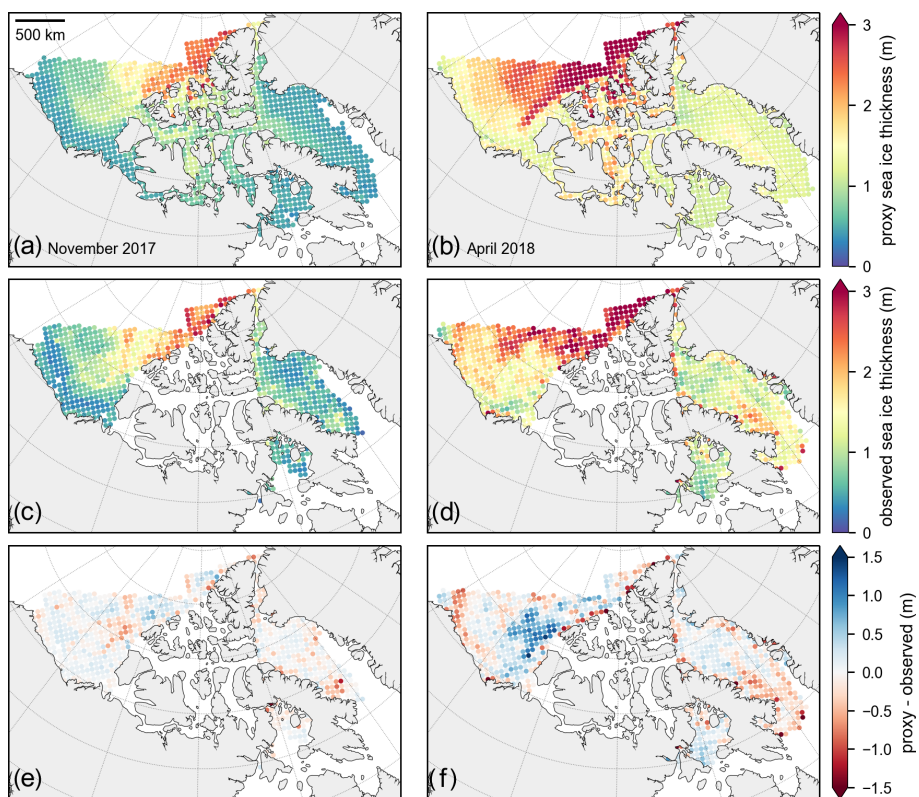
Figure 7. (a, b) Proxy sea ice thickness, **(c, d)** CryoSat-2-observed sea ice thickness, and **(e, f)** proxy-SIT-observed SIT for **(a, c, e)** November 2017 and **(b, d, f)** April 2018 when leaving the winter 2017–2018 season of CryoSat-2 ice thickness data out of the model training dataset.
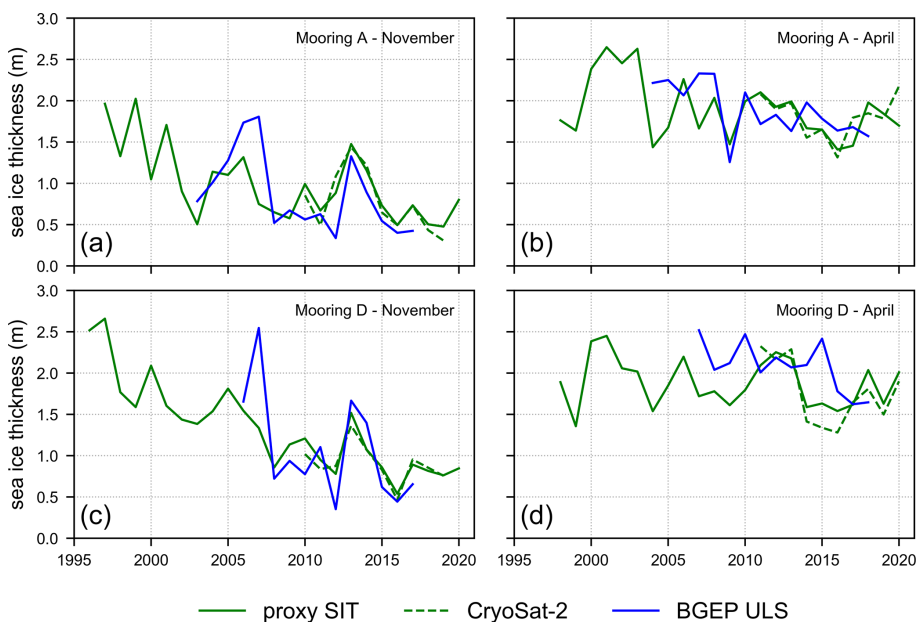

Figure 8. BGEP ULS moorings' sea ice thickness compared to the proxy_corr sea ice thickness product and CryoSat-2-observed sea ice thickness at the same location: **(a)** November mooring A, **(b)** April mooring A, **(c)** November mooring D, and **(d)** April mooring D. Locations of ULS moorings are shown in Fig. 1.
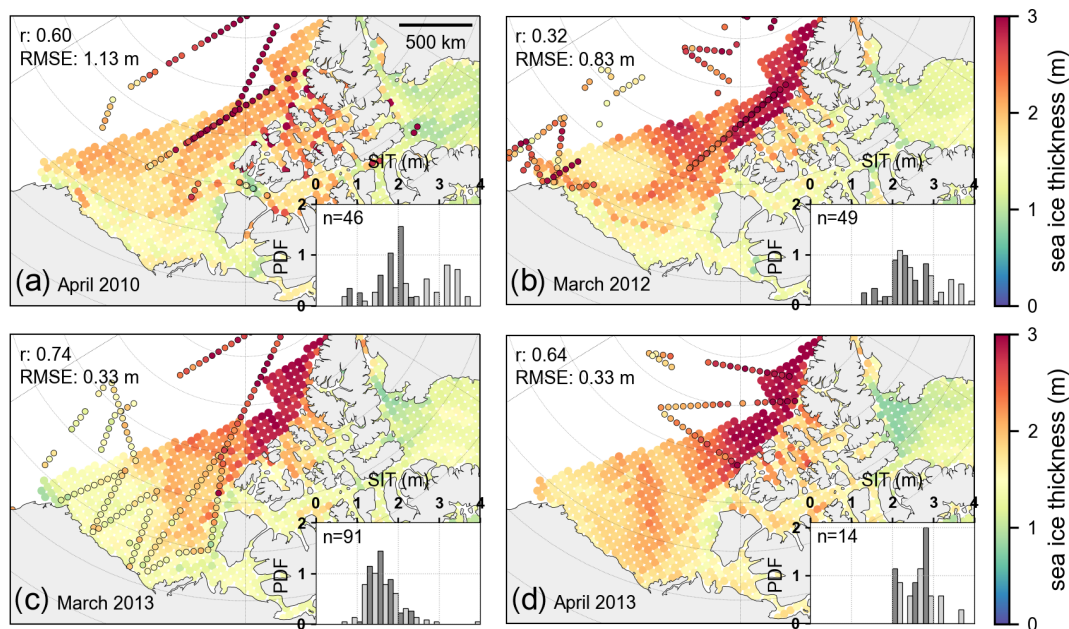
Figure 9. Operation IceBridge sea ice thickness measurements compared to the proxy_corr sea ice thickness product for **(a)** April 2010, **(b)** March 2012, **(c)** March 2013, and **(d)** April 2013. The sub-figure shows the probability density function for OIB (light grey) and the proxy SIT product (dark grey) on the OIB tracks.

years. Upon manual investigation of radar imagery of this region, the floe size does not seem smaller than in other years. This difference in floe size caused the model to predict thinner ice in April 2010 than in other years and likely led to the underestimation. This shows that the SIT proxy product created by this model is reliant on the consistency of the manually created ice charts, which, although generally robust (Tivy et al., 2011), can include anomalies.

In March 2012, the area of thick ice near the coast of Point Barrow, Alaska, observed by OIB was also observed within the CryoSat-2 SIT product but was underestimated by the proxy product. This thicker region in the OIB measurements is potentially caused by dynamic thickening of the ice pack as it converges against the coast (Fukamachi et al., 2017; Babb et al., 2020). Given that ridged ice is not classified in the ice charts, the influence of this process would not be captured by the machine-learning model, which in turn highlights one of the limitations. A similar phenomenon might be visible in April 2018 (Fig. 7), where the SIT proxy product shows thinner results than the CryoSat-2 observations in this region. For comparison, ice thickness in this region was more accurately predicted by the proxy product in March 2013 (Fig. 9c), which likely means that there was less dynamic thickening in 2013 than in 2012. Dynamic thickening of FYI during the growth season might also be the cause of the model testing error being higher in the months at the end of winter.

March and April 2013 (Fig. 9c and d) are characterized by higher correlations and lower RMSEs (0.33 m for both

March and April 2013) when comparing the proxy SIT product to OIB.

4.2.3 In situ measurements

Landfast SIT measurements at weather stations in the CAA provide a comparison to the entire record of the SIT proxy product in the Canadian Arctic channels (Fig. 10). A comparison between the fast ice thickness record and the proxy product in Cambridge Bay and Resolute gives high correlations of 0.93 and 0.73, respectively, and low RMSEs of 0.19 and 0.26 m, respectively. The weather station at Eureka provides a lower correlation (0.62) and a higher RMSE (0.36 m). However, the RMSEs of all three locations are within the uncertainty of the SIT proxy product of 0.3 to 0.5 m. The reliability of the model testing uncertainty (Fig. 5) is reinforced by the close comparisons to all three independent validation exercises here. The range of in situ field measurements in Eureka and in Cambridge Bay agrees with both the fast ice weather station measurements and the proxy SIT product (Fig. 10).

The proxy SIT product overestimates sea ice thickness at the start of winter (November and December) and underestimates sea ice thickness at the end of winter (February, March, and April) for all three locations (Fig. 10). This shows that the seasonal cycle in sea ice growth is not fully captured by the proxy SIT product in the CAA. However, it also needs to be noted that the observations at the weather stations are made in fast ice in easily accessible locations very close to shore and may not be representative of the general regional ice conditions.
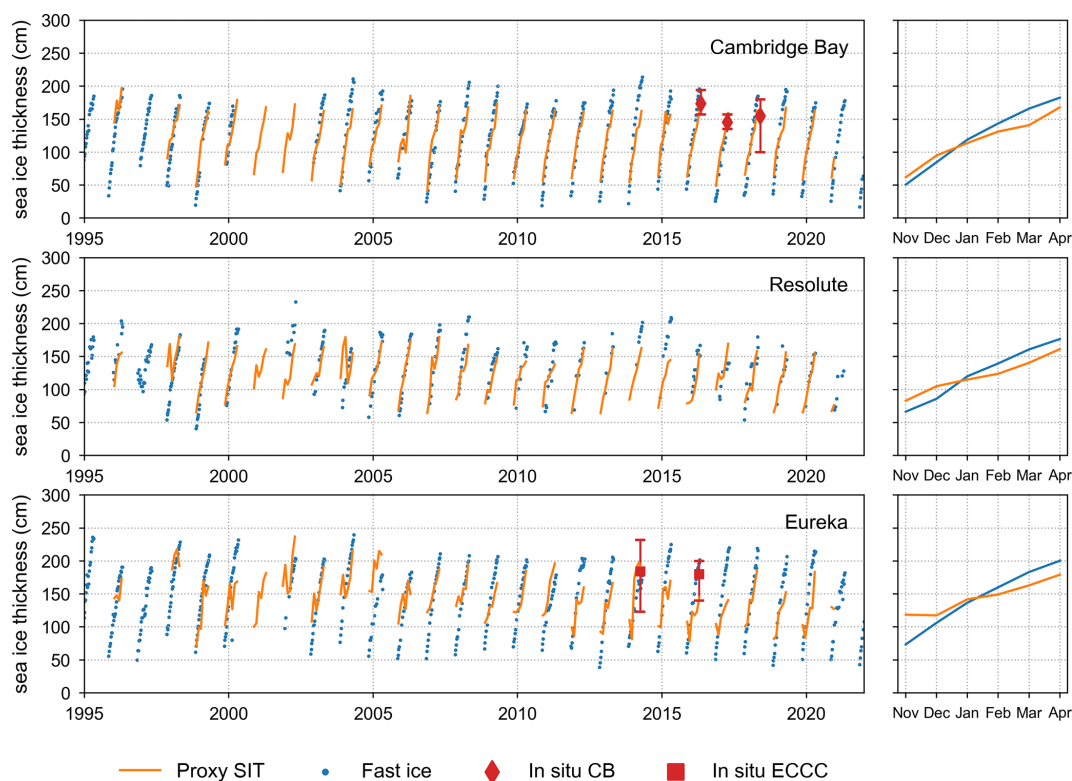
Figure 10. Fast ice thickness measurements (for the locations, see Fig. 1), the proxy_corr sea ice thickness product, and field campaign in situ observations from ECCC in Eureka (King et al., 2015, 2020) and Cambridge Bay. The graphs on the right-hand side show the mean seasonal cycle for each location.

The anomaly correlation coefficient between landfast ice measurements and the proxy product showed that the interannual variability was well captured in Cambridge Bay (ACC of 0.37) and moderately well in Eureka and Resolute (0.11 and 0.20, respectively). Again, these positive ACCs demonstrate that the directions of the interannual variations in SIT anomalies (higher or lower than usual) are typically the same between the in situ data and the proxy product. However, the magnitudes of the anomalies can be different. The ACCs are improved by 42 % on average when using the ice-type-corrected rather than ice-type-uncorrected SIT proxy product.

The correlation and anomaly correlation between the in situ measurements and the SIT proxy product at the landfast ice weather stations are in the same range as at the ULS moorings in the Beaufort Gyre. This indicates that the proxy product can estimate SIT in the channels of the Canadian Arctic Archipelago as accurately as in the open area of the Beaufort Sea.

4.3   Limitations and potential

As the random forest regression model is trained on CryoSat-2 sea ice thickness observations, the results can only be as good as CryoSat-2 observations. This is illustrated well in Fig. 8, where the SIT proxy product does in places differ from the local ULS SIT observations but agrees well with CryoSat-2 observations in all the panels. There are known limitations to CryoSat-2 SIT retrievals – e.g. the likely incorrect assumption that the Ku-band radar signal penetrates the snow layer in all the cases (Willatt et al., 2011; Nandan et al., 2017; Stroeve et al., 2022; Nab et al., 2023), the instrument not being able to measure freeboards lower than 2.5 cm (Landy et al., 2020), and the need for a reliable snow depth product to convert from radar freeboard to SIT (Glissenaar et al., 2021) – which will propagate into this SIT proxy product.

Another limitation of the proxy product is its reliance on reliable and consistent ice charts, which are created manually by ice analysts from different data sources. The data sources available, and thus the quality of the ice charts, change over time, with a big increase in quality of the ice charts in 1996 with the introduction of RADARSAT satellite observations (Tivy et al., 2011), which is why we select 1996 as the start year of the proxy SIT product. Tivy et al. (2011) assessed the data quality of the ice charts and determined that all the regions have a high enough quality since 1996 for any statistical analysis. Nevertheless, there is some variability in the quality over time and per region, with the quality being higher in the Beaufort Sea, Baffin Bay, and Parry Channel

and slightly lower in the Arctic Ocean Periphery (Tivy et al., 2011).

The proxy SIT product has difficulty resolving sea ice thickness in heavily ridged regions, as the ice charts do not specify ridging. This is particularly true in MYI regions, as there are no sub-categories for thin or thick MYI, and the scatterometer backscatter shows no difference between thin and thick MYI. Because of this the SIT proxy struggles to capture SIT in regions with a lot of ridged MYI.

Without applying the ice type–SIT correction to the proxy product, the proxy_nocorr SIT assumes that the relation between the model features (ice type, form of ice, and scatterometer backscatter) and sea ice thickness stays constant over time. This is why the ice type–SIT correction is applied to create the proxy_corr SIT product. The proxy_corr SIT product showed better agreement with the independent SIT datasets used for validation than the proxy_nocorr SIT product, showing that applying this correction improves the results. However, the ice type–SIT correction is determined using PIOMAS, which is a sea ice model with known limitations and uncertainties. One of these limitations is that PIOMAS is known to overestimate thin ice thickness and underestimate thick ice thickness (Schweiger et al., 2011), underestimating negative trends compared to observations. For this reason the applied ice type–SIT correction might be underestimated in this study, leading to conservative trend estimations.

A potential of the presented method in retrieving the proxy sea ice thickness product is that this method can be applied to new ice charts and scatterometer data as they are released. A version of the model based solely on weekly ice charts that does not include scatterometer data, which have a delayed release, offers the potential for near-real-time estimates of sea ice thickness, though this comes with an associated 2–10 cm increase in the error.

Additionally, the new year-round sea ice thickness record from CryoSat-2 (Landy et al., 2022) creates the potential to extend this methodology and the proxy of SIT into the summer months. This does however come with its own separate challenges, including a lower number of training data due to less sea ice and a change in scatterometer backscatter with snowmelt, and is therefore not considered in this analysis.

5   Sea ice thickness proxy product (1996–2020)

Using a combination of remotely sensed sea ice products, we have created a proxy sea ice thickness record that covers the full Canadian Arctic, including the CAA, and extends back to 1996. We present a proxy_nocorr SIT product, which can be used to study sea ice thickness trends caused by changes in ice type, and a proxy_corr SIT product, which is corrected for ice type–SIT trends and can be used to research long-term sea ice thickness trends. We focus our discussion on the proxy_corr SIT product, as this showed better statistics in the

validation with the independent SIT datasets. The proxy_corr product compares well with in situ observations and captures the general spatial pattern of thicker sea ice in areas known to contain old ice (the north-eastern Beaufort Sea and the northern channels in the CAA) and thinner ice in areas that are typically ice-free during summer (i.e. the southern Beaufort Sea, Foxe Basin, and Baffin Bay) (Fig. 11). The product also highlights a general reduction in sea ice thickness over the 25-year study period (Fig. 11), though there is considerable variability in the trends, both spatially and temporally (Table 3).

The overall trends in sea ice thickness in the region show significant thinning throughout winter (Table 3). Thinning is strongest in early winter (November–January) and less pronounced in the later winter months (February–April). This indicates a later freeze-up in recent years, with thickening of the sea ice happening later in winter.

The interannual variability in the proxy product is characterized by the residual standard error (RSE), which characterizes the standard deviation of the residuals in a regression model and thus the variability from the trend:

$$\text{RSE} = \sqrt{\frac{\sum (y_i - \hat{y}_i)^2}{n - 2}}, \tag{2}$$

where y_i is the observed value of mean SIT in the proxy product for a given year, $\hat{y}_i$ is the expected value in the fitted linear regression model for the same year, and n is the number of years. In the study area, the interannual variability is largest in December, with an RSE of 13 cm. The smallest interannual variability is found in April, with an RSE of 6 cm. Of the four regions outlined in Fig. 12, the variability is largest in the Arctic Ocean Periphery, with a maximum RSE (interannual variability) in January of 46 cm. High interannual variability is also found in the channels of the Queen Elizabeth Islands in the northern part of the archipelago. The lowest interannual variability is found in Baffin Bay, with a maximum RSE in February of 12 cm.

Regionally, April SIT trends are largest in Baffin Bay and the Arctic Ocean Periphery (Fig. 12), and November SIT trends are largest in the Beaufort Sea and Arctic Ocean Periphery (Fig. 13). Trends in the CAA are variable during April but show a relatively coherent reduction in ice thickness during November (Figs. 12 and 13).

Sea ice in northern Baffin Bay shows significant ($p < 0.05$) local thinning of up to 30 cm per decade in April for the full time period (1996–2020). Sea ice thickness trends in Baffin Bay have been difficult to determine in the past because altimetry records are highly reliant on the selected snow depth record and processing methods (Glissenaar et al., 2021). All the altimetry records in spring show thinning in the North Water Polynya region in the north of Baffin Bay over the past 20 years (Glissenaar et al., 2021), agreeing with the record presented here. More uncertain are sea ice thickness trends in the southern part of Baffin Bay, where trends
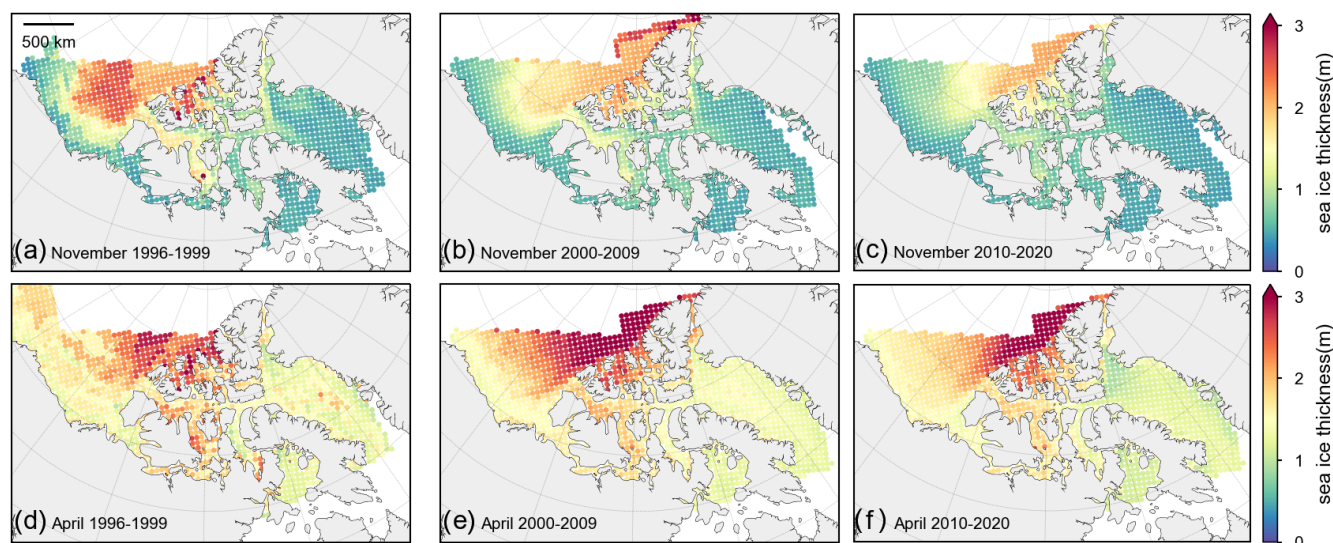
Figure 11. Decadal means from the proxy_corr sea ice thickness product for **(a, b, c)** November and **(d, e, f)** April **(a, d)** 1992–1999, **(b, e)** 2000–2009, and **(c, f)** 2010–2020.

in altimetry records are highly variable and dependent on the snow depth product applied (Glissenaar et al., 2021). The proxy SIT product presented here shows an asymmetric SIT trend in Baffin Bay, with no change in the south-west and thinning in the north and north-east. This is mostly caused by a decrease in the ice type "thick FYI" and an increase in the ice type "medium FYI" in the east and north of Baffin Bay. There is no significant change in the MYI concentration in Baffin Bay in April.

Sea ice in part of the Arctic Ocean Periphery north of the Queen Elizabeth Islands shows non-significant ice thickening in April. This thickening coincides with a non-significant increase in scatterometer backscatter and a significant but small replacement of FYI by MYI in the ice charts, so thickening could be caused by more MYI convergence against the coast (Kwok, 2015).

The Parry Channel, an important area for shipping activities, shows large yearly variability but no significant change in April (Fig. 12c). The interannual variability in the Parry Channel is linked to the variability and trends in MYI in this region. The time series of MYI in this region as shown by Howell et al. (2022) is very similar to the time series in the proxy product for SIT (Fig. 12), with a correlation between the two of $r = 0.64$. This implies that, in a heavy-MYI year, the mean ice thickness in the Parry Channel is around 2 m, whereas in a low-MYI year the mean ice thickness is around 1.5 m. This highlights the importance of MYI advection within the CAA and its role in conditioning the ice cover for the melt season and shipping season.

The end of winter (April) SIT shows non-significant thinning in the Beaufort Sea caused by a decline in the old ice concentration in the Beaufort Sea over the study period, as indicated in the old ice category of the ice charts and the scat-

terometer backscatter. This decline in old ice in the Beaufort Sea is likely caused by an increase in MYI melt in the Beaufort Sea itself, as the influx of MYI from the north has been shown to have increased (Babb et al., 2022).

Seasonally, the trends also vary by region. Baffin Bay and the Beaufort Sea have significant negative trends in SIT for almost every month in the study period in the proxy_corr product (Table 3). In the Beaufort Sea thinning is most pronounced at the start of the growth season (-28 cm per decade in November; Table 3), which is associated with a stronger negative trend in old ice in November than in April caused by greater reductions in old ice surviving the summer but a continued replenishment of old ice from the Arctic Ocean Periphery in winter (Babb et al., 2022). In Baffin Bay the thinning is more pronounced in spring (-15 cm per decade in March and April; Table 3), mostly because of strong thinning in the north of Baffin Bay, which is where the North Water Polynya is located, and corresponds to a more active polynya and greater occurrence of thin ice since the 1990s (Preußer et al., 2015). In Parry Channel thinning is only statistically significant in autumn (-18 cm per decade in November, -20 cm per decade in December), with more variability in middle and late winter. This is relevant for shipping safety as thinning of the sea ice in autumn would lengthen the summer shipping season (Howell et al., 2022; Mudryk et al., 2021). A comparison of the proxy SIT product with the Alfred Wegener Institute (AWI) CryoSat-2 SIT product (Hendricks and Paul, 2022) in the channels of the CAA (Fig. S3 in the Supplement) showed good agreement in November and a much better spatial coverage by the proxy SIT product in April. The Arctic Ocean Periphery shows no significant thinning throughout winter.
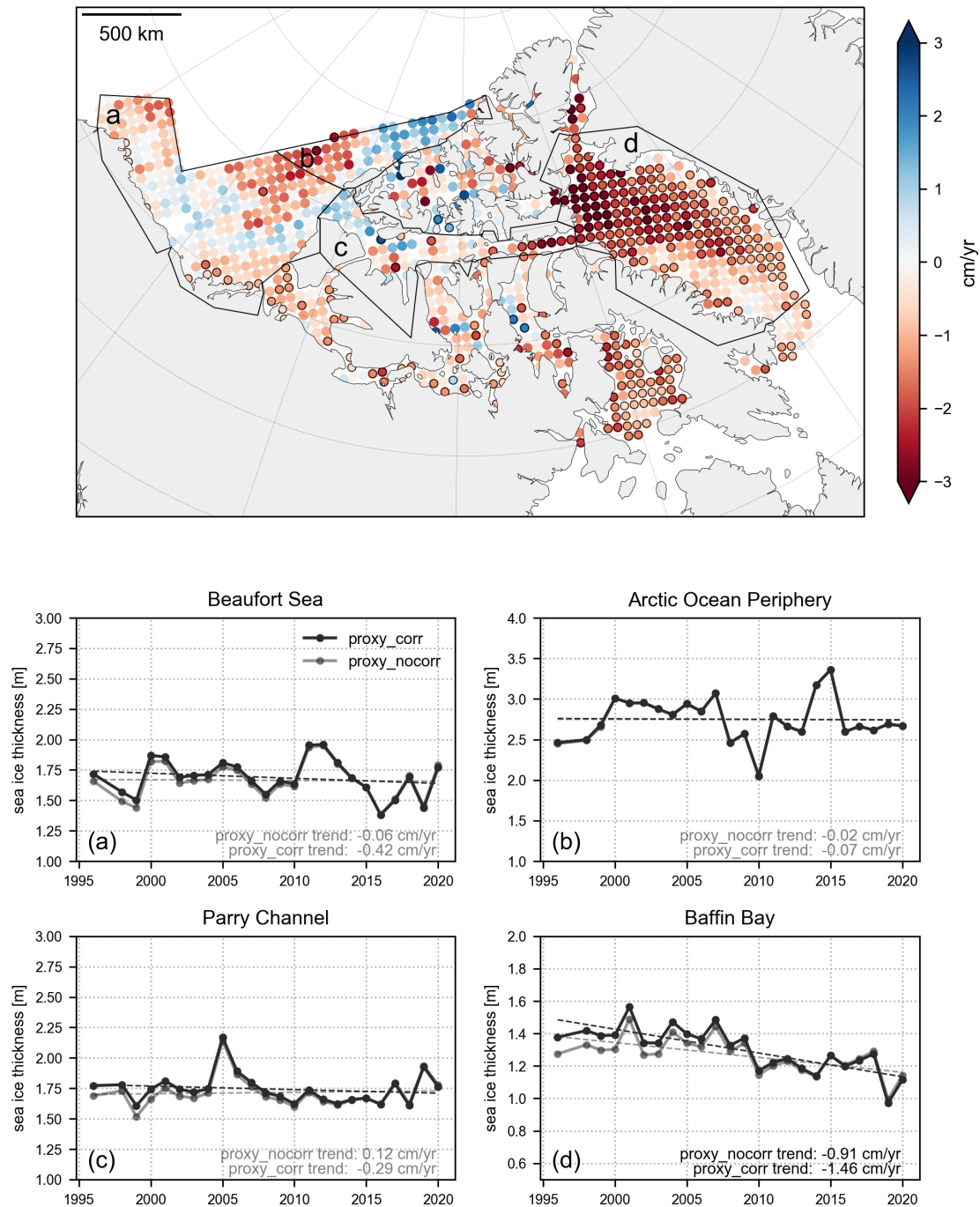
Figure 12. Sea ice thickness trends from the proxy product for April 1996–2020. The map shows trends from the proxy_corr SIT product and solid-outline circles where statistically significant ($p < 0.05$). Timelines are given for the mean of sub-regions of the Canadian Arctic (**a–d**). Trends are shown for the proxy_nocorr SIT product (light) and the proxy_corr SIT product (dark). Trend numbers are bold where significant ($p < 0.05$).

6   Conclusions

We present a proxy sea ice thickness product for the Canadian Arctic for 1996–2020 based on long-term remote-sensing records. The presented sea ice thickness proxy product estimates sea ice thickness with 30 to 50 cm testing un-

certainty, verified in a comparison with independent ice draft and thickness observations. The proxy product for SIT goes further back in time than satellite altimetry records, offering the opportunity to study trends and variability in SIT on longer timescales, and offers complete coverage of the Cana-
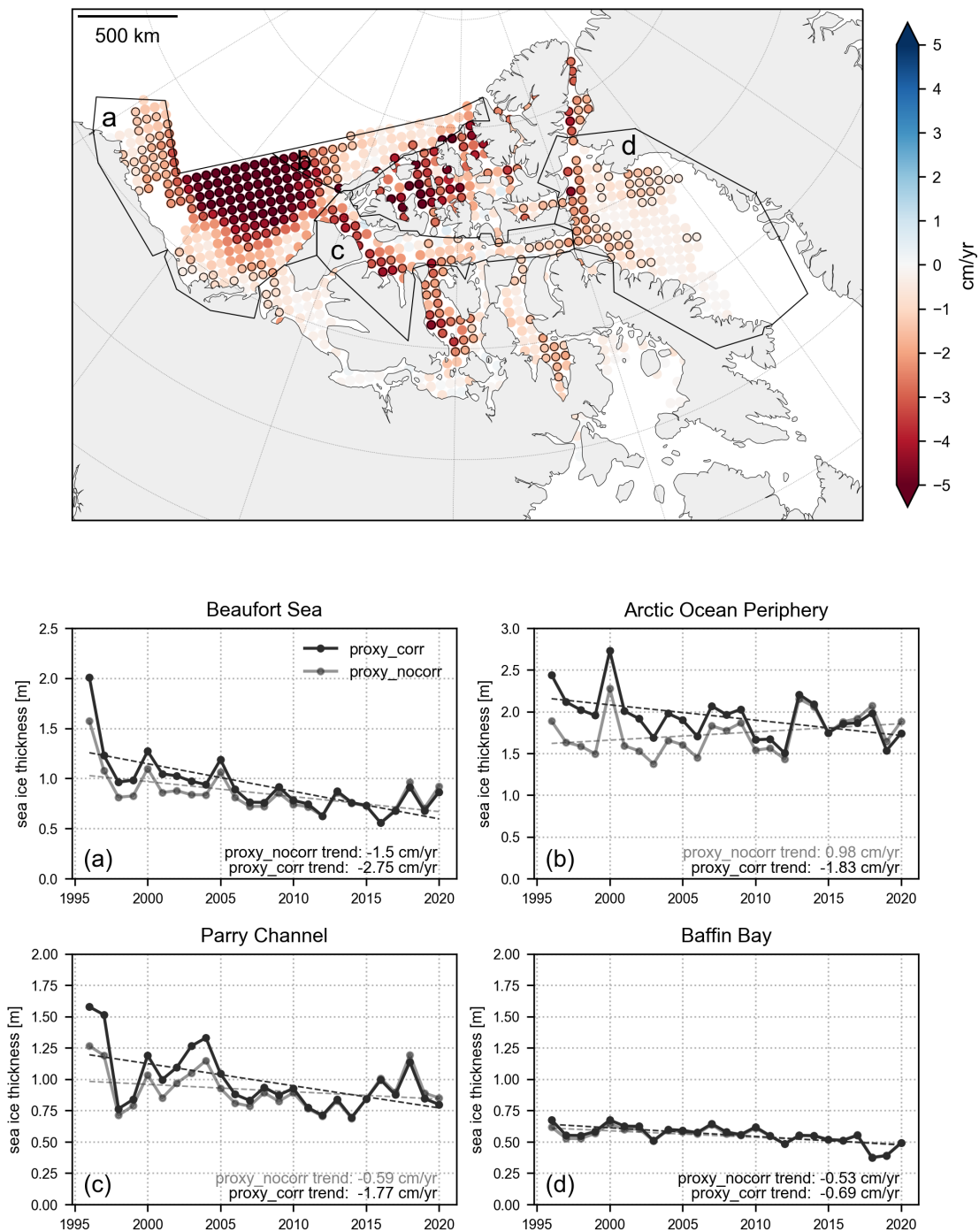
Figure 13. Same as Fig. 12 but for November.

dian Arctic, including coastal areas and the CAA, where the use of altimetry to estimate ice thickness is less certain. The presented proxy product is the first large-scale SIT product reliably covering the complex CAA channels.

The sea ice thickness proxy product shows that sea ice is thinning over most of the Canadian Arctic, with a mean trend over the full area of $-0.82\,\mathrm{cm\,yr^{-1}}$ in April. The trends vary

locally and throughout winter. The Beaufort Sea and Baffin Bay show significant thinning during all the months, while the Arctic Ocean Periphery shows negative trends during all the months but January and March, and Parry Channel shows negative trends during November and December. Thinning in the Beaufort Sea peaks at $-2.8\,\mathrm{cm\,yr^{-1}}$ in autumn (November), whereas Baffin Bay shows the strongest thinning in

Table 3. Sea ice thickness trends for proxy_nocorr and proxy_corr in Canadian Arctic sub-regions for 1996–2020 (cm yr^{-1}). Sub-region outlines are shown in Figs. 12 and 13. Bold where significant ($p < 0.05$).

		Beaufort Sea	Arctic Ocean Periphery	Parry Channel	Baffin Bay	Full study area
November	proxy_nocorr	**−1.50**	0.98	−0.59	**−0.53**	**−0.67**
	proxy_corr	**−2.75**	**−1.83**	**−1.77**	**−0.69**	**−1.54**
December	proxy_nocorr	−0.34	−0.29	−0.16	−0.26	−0.57
	proxy_corr	**−2.11**	**−3.87**	**−2.04**	-0.93	**−2.11**
January	proxy_nocorr	**−1.18**	0.54	0.61	−0.47	−0.47
	proxy_corr	**−2.54**	−2.05	−0.57	**−0.96**	**−1.48**
February	proxy_nocorr	**−0.77**	−0.57	0.26	−0.65	−0.44
	proxy_corr	**−1.85**	**−2.26**	−0.70	**−1.30**	**−1.34**
March	proxy_nocorr	**−0.86**	0.44	0.27	**−1.00**	**−0.57**
	proxy_corr	**−1.75**	−0.98	−0.47	**−1.54**	**−1.31**
April	proxy_nocorr	−0.06	0.02	0.12	**−0.91**	−0.38
	proxy_corr	−0.42	−0.07	−0.29	**−1.46**	**−0.82**

spring (-1.5 cm yr^{-1} in April). The Arctic Ocean Periphery shows the highest interannual variability. Thinning in Parry Channel peaks during autumn (-2.0 cm yr^{-1} in December).

The SIT proxy product can be used to study long-term trends and variability in SIT in the Canadian Arctic, to monitor SIT for shipping safety purposes, and to initialize and verify seasonal prediction models. The product can also be used as a reference or in models for studying other features in this area that are affected by SIT change, e.g. research on primary productivity and microbial life (Post et al., 2013; Campbell et al., 2022), the effect of oil pollution (Redmond Roche and King, 2022), and the surface energy balance (Ledley, 1988). Lastly, the random forest regression can be applied in near real time to estimate ice thickness from ice charts and scatterometer data and to extend the proxy SIT product into the future.

Appendix A: Scatterometer record

One of the features used in the random forest regression model is scatterometer data. As there is no continuous record of one instrument over the entire 1996–2020 record, we use data of multiple instruments. We have used data from both C-band and Ku-band scatterometer instruments. C-band scatterometers work in the 4–8 GHz frequency range and Ku-band scatterometers in the 12–18 GHz frequency range. As these wavelengths interact differently with snow and ice (Ontstott, 1992), we expect C-band and Ku-band instruments to give different results and do not combine scatterometer data from the different bands into one record. Instead, we create a C-band record combining ERS-1, ERS-2, and AS-CAT and a Ku-band record combining QuikSCAT, OSCAT-1, and OSCAT-2 (Fig. 3). This section discusses why we believe these records can be combined.

NASA's QuikSCAT (Quick Scatterometer) was an Earth observation satellite carrying the Ku-band (13.4 GHz) dual-polarization scatterometer SeaWinds. QuikSCAT was launched on 19 June 1999 and stopped collecting data on 21 November 2009. Daily horizontal-polarization gridded data were retrieved from the NASA SCP for 1 July 1999 to 21 November 2009 (https://www.scp.byu.edu/data/Quikscat/SIRv2/Quikscat_sirV2.html, last access: 22 February 2022).

The Indian Space Research Organisation (ISRO) OSCAT-1 scatterometer was carried by Oceansat-2 and operated in the Ku band (13.515 GHz). The instrument provides daily global coverage at a resolution of 25 km. Horizontal-polarization gridded scatterometer data were retrieved from the NASA SCP for 5 November 2009 to 21 February 2014 (https://www.scp.byu.edu/data/OSCAT/SIR/OSCAT_sir.html, last access: 22 February 2022). The follow-on mission ScatSat-1 carried OSCAT-2. Daily horizontal-polarization data were obtained from the Meteorological and Oceanographic Satellite Data Archival Centre (MOSDAC) for 1 November 2016 to 31 December 2020 (https://mosdac.gov.in/satellite-catalog, last access: 10 February 2022).

The Ku-band record consists of QuikSCAT (data from the NASA SCP available for August 1999 to 23 November 2009), OSCAT-1 (data available for 5 November 2009 to 21 February 2014), and OSCAT-2 (data from MOSDAC available for November 2016 to the present). OSCAT-1 and OSCAT-2 are similar instruments. The NASA SCP OSCAT-2 dataset is only available until 2019, so we decided to use the MOSDAC OSCAT-2 dataset. OSCAT-1 and OSCAT-2 do not have a temporal overlap, so a direct comparison is not possible. Figure A1 shows that the seasonal cycle of the retrieved backscatter signal is very comparable between the two products, so we do not apply a bias correction and assume that
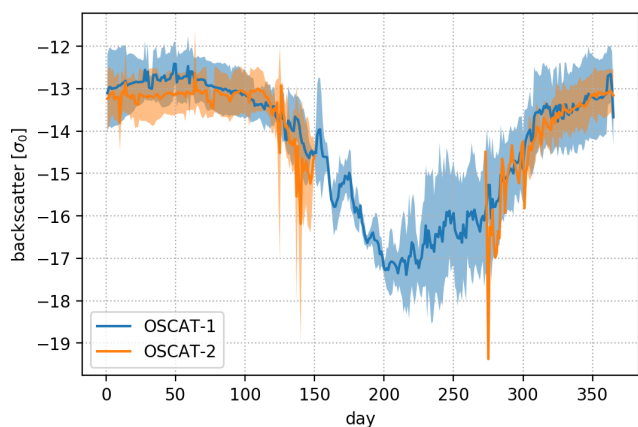
Figure A1. Seasonal cycle of scatterometer backscatter from OSCAT-1 and OSCAT-2.

Figure A2. Backscatter from OSCAT-1 and QuikSCAT for the overlapping period (5–23 November 2009).

the records can be combined. OSCAT and QuikSCAT are very similar instruments. OSCAT measurements are at a slightly different incidence angle than QuikSCAT. OSCAT-1 and QuikSCAT have a 19 d temporal overlap in November 2009. The backscatters from both instruments in this period are compared (Fig. A2) and deemed similar enough to combine the record.

ERS-1 was a European Space Agency (ESA) spacecraft launched on 17 July 1991 to provide microwave-spectrum-based environmental monitoring. The spacecraft carried a range of instruments, including the wind scatterometer and SAR instruments, which worked in tandem in a configuration called the Active Microwave Instrument (AMI). The instrument measures the C band at a frequency of 5.3 GHz and has a spatial resolution of about 50 km. The ERS-1 mission ended on 10 March 2000. Gridded ERS-1 scatterometer data were retrieved from the NASA SCP for 1 January 1996 to 2 May 1996 (https://www.scp.byu.edu/data/ERS/SIR/ERS_sir.html, lsat access: 24 February 2022). ERS-2 was launched in the same orbit as ERS-1 on 21 April 1995 and carried the same instruments as ERS-1. ERS-2 was taken out of service on 5 September 2011. Gridded ERS-2 scatterometer data for 1 June 1996 to 18 January 2001 were also retrieved from the NASA SCP (https://www.scp.byu.edu/data/ERS/SIR/ERS_sir.html).

The Advanced Scatterometer (ASCAT) is a C-band (5.255 GHz) advanced version of the AMI flown on ERS-1 and ERS-2. ASCAT was carried by the ESA's Meteorological operational satellite A (MetopA), which was part of the EUMETSAT Polar System, together with Metop-B and Metop-C. Metop-A was launched on 19 October 2006 and retired on 15 November 2021. Metop-B and Metop-C were launched in 2012 and 2018, respectively, and are still operational. They provide global coverage in 1.5 d and have a 12.5 km spatial resolution. ASCAT's vertical-polarization scatterometer gridded data were retrieved from the NASA SCP for 1 Jan-
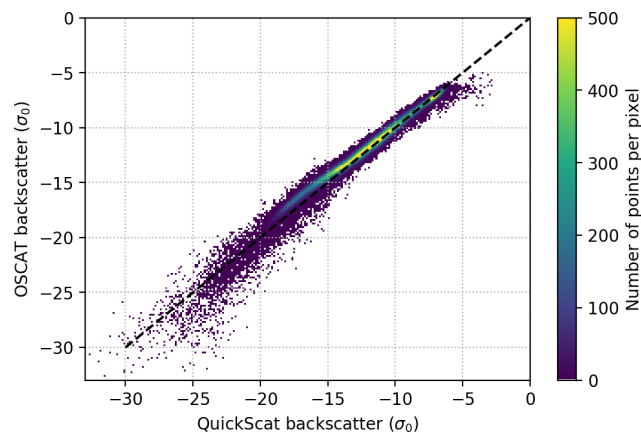
uary 2007 to 31 December 2020 (https://www.scp.byu.edu/data/Ascat/SIR/Ascat_sir.html, last access: 1 June 2023).

The C-band record consists of ERS-1 (data from the NASA SCP available for January 1992 to April 1996), ERS-2 (data available June 1996 to mid-January 2001), and ASCAT (January 2007 to the present). ERS-1 and ERS-2 are designed to be identical twins, with the same scatterometer instrument and flying in the same orbit. They can thus be applied together. ASCAT differs from ERS in its higher observation density, better noise characteristics, and slightly higher incidence angles. As we use a low-resolution product for the scatterometer data (GRD – gridded data image), we believe that the difference in noise is removed. The lower observation density of ERS is no issue because only monthly data are used. There is no temporal overlap in ERS-2 and ASCAT, so a direct assessment of their comparison is not possible. As the period between ERS-2 and ASCAT has seen a decline in older ice, we do not expect the scatterometer data to be directly comparable. We have compared the backscatter results for ERS-2 and ASCAT for different ice ages (obtained from the EASE-grid Sea Ice Age product from NSIDC, https://nsidc.org/data/nsidc0611/versions/4, last access: 21 January 2022) and shown that the backscatter distribution for ice of the same age is similar for ERS-2 and ASCAT (Fig. A3).
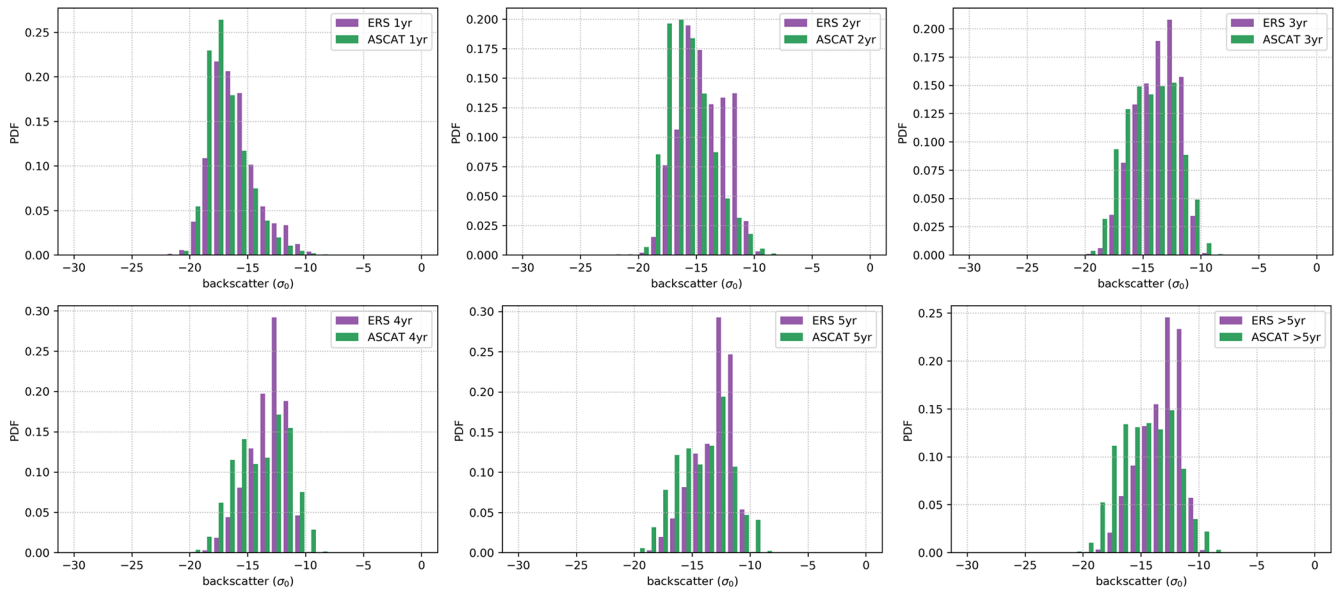
Figure A3. Probability density function of backscatter on different ice ages for ERS-2 and ASCAT.

Author contributions. IAG conceptualized the study, carried out the main analysis, and wrote the paper. JCL provided the SIT from CryoSat-2 and helped develop the methodology. JCL, DGB, GJD, and SELH contributed to the interpretation of the results. All the authors contributed to revising and improving the manuscript.

References

Aldenhoff, W., Heuzé, C., and Eriksson, L. E. B.: Sensitivity of radar altimeter waveform changes in sea ice type at resolution of Synthetic Aperture Radar, Remote Sens., 11, 22, https://doi.org/10.3390/rs11222602, 2019.

Alexandrov, V., Sandven, S., Wahlin, J., and Johannessen, O. M.: The relation between sea ice thickness and freeboard in the Arc-

tic, The Cryosphere, 4, 373–380, https://doi.org/10.5194/tc-4-373-2010, 2010.

Babb, D. G., Landy, J. C., Barber, D. G., and Galley, R. J.: Winter sea ice export from the Beaufort Sea as a pre-conditioning mechanism for enhanced summer melt: a case study of 2016, J. Geophys. Res.-Oceans, 124, 6575–6600, https://doi.org/10.1029/2019JC015053, 2019.

Babb, D. G., Landy, J. C., Lukovich, J. V., Haas, C., Hendricks, S., Barber, D. G., and Galley, R. J.: The 2017 reversal of the Beaufort Gyre: can dynamic thickening of seasonal ice cover during a reversal limit summer ice melt in the Beaufort Sea, J. Geophys. Res.-Oceans, 125, e2020JC016796, https://doi.org/10.1029/2020JC016796, 2020.

Babb, D. G., Galley, R. J., Howell, S. E. L., Landy, J. C., Stroeve, J. C., and Barber, D. G.: Increasing multiyear sea ice loss in the Beaufort Sea: a new export pathway for the diminishing multiyear ice cover of the Arctic Ocean, Geophys. Res. Lett., 49, e2021GL097595, https://doi.org/10.1029/2021GL097595, 2022.

Barber, D., Babb, D., Ehn, J., Chan, W., Matthes, L., Dalman, L., Campbell, Y., Harasyn, M., Firoozy, N., Theriault, N., Lukovich, J., Zagon, T., Papakyriakou, T., Capelle, D., Forest, A., and Gariepy, A.: Increasing mobility of high Arctic sea ice increases marine hazards off the east coast of Newfoundland, Geophys. Res. Lett., 45, 2370–2379, https://doi.org/10.1002/2017GL076587, 2018.

Belmonte Rivas, M., Otosaka, I., Stoffelen, A., and Verhoef, A.: A scatterometer record of sea ice extents and backscatter: 1992–2016, The Cryosphere, 12, 2941–2953, https://doi.org/10.5194/tc-12-2941-2018, 2018.

Bourke, R. and Garrett, R.: Sea ice thickness distribution in the Arctic Ocean, Cold Reg. Sci. Technol., 13, 259–280, https://doi.org/10.1016/0165-232X(87)90007-3, 1987.

Brown, R. and Cote, P.: Interannual variability of landfast ice thickness in the Canadian High Arctic, 1950–89, Arctic, 45, 273–284, 1992.

Campbell, K., Matero, I., Bellas, C., Turpin-Jelfs, T., Anhaus, P., Graeve, M., Fripiat, F., Tranter, M., Landy, J. C., Sanchez-Baracaldo, P., Leu, E., Katlein, C., Mundy, C. J., Rysgaard, S., Tedesco, L., Haas, C., and Nicolaus, M.: Monitoring a changing Arctic: Recent advancements in the study of sea ice microbial communities, Ambio, 51, 318–332, https://doi.org/10.1007/s13280-021-01658-z, 2022.

Canadian Ice Service (CIS): Regional charts: History, accuracy, and caveats, Tech. rep., Canadian Ice Service Archive Doc. Ser. 1, Gatineau, Quebec, Canada, http://ice.ec.gc.ca/IA_DOC/cisads_no_001_e.pdf (last access: 5 August 2023), 2007a.

Canadian Ice Service (CIS): Regional charts: Canadian Ice Service Ice Regime Regions (CISIRR) and sub-regions with associated data quality indices, Tech. rep., canadian Ice Service Archive Doc. Ser. 3, Gatineau, Quebec, Canada, http://ice.ec.gc.ca/IA_DOC/cisads_no_003_e.pdf (last access: 5 August 2023), 2007b.

Dawson, J., Carter, N. A., van Luijk, N., Weber, M., and Cook, A.: Arctic corridors and northern voices project: Methods for community-based participatory mapping for low impact shipping corridors in Arctic Canada, MethodsX, 7, 101064, https://doi.org/10.1016/j.mex.2020.101064, 2020.

Derksen, C., Burgess, D., Duguay, C., Howell, S., Mudryk, L., Smith, S., Thackeray, C., and Kirchmeier-Young, M.: Changes in snow, ice, and permafrost across Canada: Chapter 5, in: Canada's Changing Climate Report, edited by: Bush, E. and Lemmen, D., Government of Canada, Ottowa, ISBN 978-0-660-30222-5, 2018.

Early, D. and Long, D.: Image reconstruction and enhanced resolution from irregular shape, IEEE T. Geosci. Remote, 39, 291–302, 2001.

Fetterer, F., Savoie, M., Helfrich, S., and Clemente-Colón, P.: Multisensor Analyzed Sea Ice Extent – Northern Hemisphere (MASIE-NH), Version 1, Boulder, Colorado USA, National Snow and Ice Data Center [data set], https://doi.org/10.7265/N5GT5K3K, 2010.

Fukamachi, Y., Simizu, D., Ohshima, K. I., Eicken, H., Mahoney, A. R., Iwamoto, K., Moriya, E., and Nihashi, S.: Sea-ice thickness in the coastal northeastern Chukchi Sea from moored ice-profiling sonar, J. Glaciol., 63, 888–898, https://doi.org/10.1017/jog.2017.56, 2017.

Galley, R. J., Babb, D., Ogi, M., Else, B. G. T., Geilfus, N.-X., Crabeck, O., Barber, D. G., and Rysgaard, S.: Replacement of multiyear sea ice and changes in the open water season duration inthe Beaufort Sea since 2004, J. Geophys. Res.-Oceans, 121, 1806–1823, https://doi.org/10.1002/2016JC012132, 2016.

Géron, A.: Hands-on machine learning with scikit-learn, Keras and Tensorflow, O'Reilly Media, Inc., Sebastopol, USA, 2nd Edn., ISBN 978-1-492-03264-9, 2019.

Glissenaar, I., Landy, J., Babb, D., Dawson, G., and Howell, S.: IsoldeGlissenaar/seaiceproxy: Proxy SIT Canadian Arctic, Zenodo [code], https://doi.org/10.5281/zenodo.7625422, 2023a.

Glissenaar, I., Landy, J., Babb, D., Dawson, G., and Howell, S.: IsoldeGlissenaar/CanadianSITproxy: Proxy SIT Canadian Arctic, Zenodo [data set], https://doi.org/10.5281/zenodo.7644084, 2023b.

Glissenaar, I. A., Landy, J. C., Petty, A. A., Kurtz, N. T., and Stroeve, J. C.: Impacts of snow data and processing methods on the interpretation of long-term changes in Baffin Bay early spring sea ice thickness, The Cryosphere, 15, 4909–4927, https://doi.org/10.5194/tc-15-4909-2021, 2021.

Haas, C. and Howell, S.: Ice thickness in the Northwest Passage, Geophys. Res. Lett., 42, 7673–7680, https://doi.org/10.1002/2015GL065704, 2015.

Haas, C., Hendricks, S., Eicken, H., and Herber, A.: Synoptic airborne thickness surveys reveal state of Arctic sea ice cover, Geophys. Res. Lett., 37, L09501, https://doi.org/10.1029/2010GL042652, 2010.

Hendricks, S. and Paul, S.: Product Users Guide & Algorithm Specification: AWI CryoSat-2 Sea Ice Thickness (version 2.5), Zenodo, https://doi.org/10.5281/zenodo.7416200, 2022.

Howell, S., Tivy, A., Agnew, T., Markus, T., and Derksen, C.: Extreme low sea ice years in the Canadian Arctic Archipelago: 1998 versus 2007, J. Geophys. Res.-Oceans, 115, C10053, https://doi.org/10.1029/2010JC006155, 2010.

Howell, S. E. L., Brady, M., Derksen, C., and Kelly, R. E. J.: Recent changes in sea ice area flux through the Beaufort Sea during the summer, J. Geophys. Res.-Oceans, 121, 2659–2672, https://doi.org/10.1002/2015JC011464, 2016.

Howell, S. E. L., Brady, M., and Komarov, A. S.: Generating large-scale sea ice motion from Sentinel-1 and the RADARSAT Constellation Mission using the Environment and Climate Change Canada automated sea ice tracking system, The Cryosphere, 16, 1125–1139, https://doi.org/10.5194/tc-16-1125-2022, 2022.

Hwang, B., Wilkinson, J., Maksym, T., Graber, H. C., Schweiger, A., Horvat, C., Perovich, D. K., Arntsen, A. E., Timothy, P., Ren, J., and Wadhams, P.: Winter-to-summer transition of Arctic sea ice breakup and floe size distribution in the Beaufort Sea, Elementa, 5, 40, https://doi.org/10.1525/elementa.232, 2017.

Kacimi, S. and Kwok, R.: Arctic Snow Depth, Ice Thickness, and Volume From ICESat-2 and CryoSat-2: 2018–2021, Geophys. Res. Lett., 49, e2021GL097448, https://doi.org/10.1029/2021GL097448, 2022.

King, J., Howell, S., Derksen, C., Rutter, N., Toose, P., Beckers, J. F., Haas, C., Kurtz, N., and Richter-Menge, J.: Evaluation of Operation IceBridge quick-look snow depth estimates on sea ice, Geophys. Res. Lett., 42, 9302–9310, https://doi.org/10.1002/2015GL066389, 2015.

King, J., Howell, S., Brady, M., Toose, P., Derksen, C., Haas, C., and Beckers, J.: Local-scale variability of snow density on Arctic sea ice, The Cryosphere, 14, 4323–4339, https://doi.org/10.5194/tc-14-4323-2020, 2020.

Krishfield, R. and Proshutinsky, A.: BGOS ULS Data Processing Procedure, Tech. rep., Woods Holde Oceanographic Institution, Falmouth, MA, USA, https://www2.whoi.edu/site/beaufortgyre/wp-content/uploads/sites/108/2020/04/BGOS_ULS_Data_Processing_Procedure_85684.pdf (last access: 7 June 2022), 2006.

Krishfield, R., Proshutinsky, A., Tateyama, K., Williams, W. J., Camack, E. C., McLauglin, F. A., and Timmermans, M.-L.: Deterioration of perennial sea ice in the Beaufort Gyre from 2003 to 2012 and its impact on the oceanic freshwater cycle, J. Geophys. Res.-Oceans, 119, 1271–1305, https://doi.org/10.1002/2013JC008999, 2014.

Kurtz, N., Studinger, M., Harbeck, J., Onana, V., and Yi, D.: IceBridge L4 Sea Ice Freeboard, Snow-Depth, and Thickness Version 1, National Snow and Ice Data Center [data set], https://doi.org/10.5067/G519SHCKWQV6, 2015.

Kwok, R.: Sea ice convergence along the Arctic coasts of Greenland and the Canadian Arctic Archipelago: variability and extremes (1992–2014), Geophys. Res. Lett., 42, 7598–7605, https://doi.org/10.1002/2015GL065462, 2015.

Landy, J. C., Petty, A. A., Tsamados, M., and Stroeve, J. C.: Sea ice roughness overlooked as a key source of uncertainty in CryoSat-2 ice freeboard retrievals, J. Geophys. Res.-Oceans, 125, e2019JC015820, https://doi.org/10.1029/2019JC015820, 2020.

Landy, J. C., Dawson, G. J., Tsamados, M., Bushuk, M., Stroeve, J. C., Howell, S. E. L., Krumpen, T., Babb, D. G., Komarov, A. S., Heorton, H. D. B. S., Belter, H. J., and Aksenov, Y.: A year-round satellite sea-ice thickness record from CryoSat-2, Nature, 609, 517–522, https://doi.org/10.1038/s41586-022-05058-5, 2022.

Ledley, T. S.: A coupled energy balance climate-sea ice model: impact of sea ice and leads on climate, J. Geophys. Res., 93, 15919–15932, https://doi.org/10.1029/jd093id12p15919, 1988.

Lietaer, O., Fichefet, T., and Legat, V.: The effects of resolving the Canadian Arctic Archipelago in a finite element sea ice model, Ocean Model., 24, 140–152, https://doi.org/10.1016/j.ocemod.2008.06.002, 2008.

Lindell, D. B. and Long, D. G.: Multiyear Arctic ice classification using ASCAT and SSMIS, Remote Sens., 8, 5, https://doi.org/10.3390/rs8040294, 2016.

Liston, G. E., Itkin, P., Stroeve, J., Tschudi, M., Stewart, J. S., Pedersen, S. H., Reinking, A. K., and Elder, K.: A Langrangian snow-evolution system for sea-ice applications (SnowModel-LG): Part I – Model Description, J. Geophys. Res.-Oceans, 125, e2019JC015913, https://doi.org/10.1029/2019JC015913, 2020.

Liu, Y., Key, J. R., Wang, X., and Tschudi, M.: Multidecadal Arctic sea ice thickness and volume derived from ice age, The Cryosphere, 14, 1325–1345, https://doi.org/10.5194/tc-14-1325-2020, 2020.

Marshall, J. and Schott, F.: Open-Ocean Convection: Observations, theory and models, Rev. Geophys., 37, 1–64, https://doi.org/10.1029/98RG02739, 1999.

Maslanik, J. A., Fowler, C., Stroeve, J., Drobot, S., Zwally, J., Yi, D., and Emery, W.: A younger, thinner Arctic ice cover: Increased potential for rapid, extensive sea-ice loss, Geophys. Res. Lett., 34, L24501, https://doi.org/10.1029/2007GL032043, 2017.

Melling, H.: Sea ice of the northern Canadian Arctic Archipelago, J. Geophys. Res., 107, 3181, https://doi.org/10.1029/2001JC001102, 2002.

Melling, H.: Thickness of multi-year sea ice on the northern Canadian polar shelf: a second look after 40 years, The Cryosphere, 16, 3181–3197, https://doi.org/10.5194/tc-16-3181-2022, 2022.

Melling, H., Agnew, T. A., Flakner, K. K., Greenberg, D. A., Lee, C. M., Münchow, A., Petrie, B., Prinsenberg, S. J., Samelson, R. M., and Woodgate, R. A.: Fresh-water fluxes via Pacific and Arctic outflows across the Canadian Polar Shelf, in: Arctic-Subarctic Ocean Fluxes, edited by: Dickson, R. R., Meincke, J., and Rhines, P., Springer, Dordrecht, https://doi.org/10.1007/978-1-4020-6774-7_10, 2008.

Melling, H., Haas, C., and Brossier, E.: Invisible polynyas: Modulation of fast ice thickness by ocean heat flux on the Canadian polar shelf, J. Geophys. Res.-Oceans, 120, 777–795, https://doi.org/10.1002/2014JC010404, 2015.

Mudryk, L. R., Derksen, C., Howell, S., Laliberté, F., Thackeray, C., Sospedra-Alfonso, R., Vionnet, V., Kushner, P. J., and Brown, R.: Canadian snow and sea ice: historical trends and projections, The Cryosphere, 12, 1157–1176, https://doi.org/10.5194/tc-12-1157-2018, 2018.

Mudryk, L. R., Dawson, J., Howell, S. E., Derksen, C., Zagon, T. A., and Brady, M.: Impact of 1, 2 and 4 °C of global warming on ship navigation in the Canadian Arctic, Nat. Clim. Change, 11, 673–679, https://doi.org/10.1038/s41558-021-01087-6, 2021.

Nab, C., Mallett, R., Gregory, W., Landy, J., Lawrence, I., Willatt, R., Stroeve, J., and Tsamados, M.: Synoptic variability in satellite altimeter-derived radar freeboard of Arctic sea ice, Geophys. Res. Lett., 50, e2022GL100696, https://doi.org/10.1029/2022GL100696, 2023.

Nandan, V., Geldsetzer, T., Yackel, J., Scharien, R., Howell, S., King, J., Ricker, R., and Else, B.: Effect of snow salinity on CryoSat-2 Arctic first-year sea ice freeboard measurements, Geophys. Res. Lett., 44, 10419–10426, 2017.

Ontstott, R. G.: SAR and scatterometer signatures of sea ice, in: Microwave Remote Sensing of Sea Ice, edited by: Carsey, F. D., vol. 68, American Geophysical Union, Geophysical Monograph Series, Wiley, Hoboken, USA, https://doi.org/10.1029/GM068, 1992.

Petty, A. A., Hutchings, J. K., Richter-Menge, J. A., and Tschudi, M. A.: Sea ice circulation around the Beaufort Gyre: The changing role of wind forcing and the

sea ice state, J. Geophys. Res.-Oceans, 121, 3278–3296, https://doi.org/10.1002/2015JC010903, 2016.

Pizzolato, L., Howell, S., Derksen, C., Dawson, J., and Copland, L.: Changing sea ice conditions and marine transportation activity in Canadian Arctic waters between 1990 and 2012, Climatic Change, 123, 161–173, https://doi.org/10.1007/s10584-013-1038-3, 2014.

Post, E., Bhatt, U. S., Bitz, C. M., Brodie, J. F., Fulton, T. L., Hebblewhite, M., Kerby, J., Kutz, S. J., Stirling, I., and Walker, D. A.: Ecological Consequences of Sea-Ice Decline, Science, 341, 519–525, https://doi.org/10.1126/science.1235225, 2013.

Preußer, A., Heinemann, G., Willmes, S., and Paul, S.: Multidecadal variability of polynya characteristics and ice production in the North Water Polynya by means of Passive Microwave and Thermal Infrared satellite imagery, Remote Sens., 7, 15844–15867, https://doi.org/10.3390/rs71215807, 2015.

Redmond Roche, B. H. and King, M. D.: Quantifying the effects of background concentrations of crude oil pollution on sea ice albedo, The Cryosphere, 16, 3949–3970, https://doi.org/10.5194/tc-16-3949-2022, 2022.

Ricker, R., Hendricks, S., Helm, V., Skourup, H., and Davidson, M.: Sensitivity of CryoSat-2 Arctic sea-ice freeboard and thickness on radar-waveform interpretation, The Cryosphere, 8, 1607–1622, https://doi.org/10.5194/tc-8-1607-2014, 2014.

Schweiger, A., Lindsay, R., Zhang, J., Steele, M., Stern, H., and Kwok, R.: Uncertainty in modeled Arctic sea ice volume, J. Geophys. Res.-Oceans, 116, C00D06, https://doi.org/10.1029/2011JC007084, 2011.

Stroeve, J., Liston, G., Buzzard, S., Zhou, L., Mallett, R., Barrett, A., Tschudi, M., Tsamados, M., Itkin, P., and Stewart, J.: A Langrangian snow-evolution system for sea-ice applications (SnowModel-LG): Part II – Analyses, J. Geophys. Res.-Oceans, 125, e2019JC015913, https://doi.org/10.1029/2019JC015913, 2020.

Stroeve, J., Nandan, V., Willatt, R., Dadic, R., Rostosky, P., Gallagher, M., Mallett, R., Barrett, A., Hendricks, S., Tonboe, R., McCrystall, M., Serreze, M., Thielke, L., Spreen, G., Newman, T., Yackel, J., Ricker, R., Tsamados, M., Macfarlane, A., Hannula, H.-R., and Schneebeli, M.: Rain on snow (ROS) understudied in sea ice remote sensing: a multi-sensor analysis of ROS during MOSAiC (Multidisciplinary drifting Observatory for the Study of Arctic Climate), The Cryosphere, 16, 4223–4250, https://doi.org/10.5194/tc-16-4223-2022, 2022.

Tilling, R., Ridout, A., and Shepherd, A.: Assessing the Impact of Lead and Floe Sampling on Arctic Sea Ice Thickness Estimates from Envisat and CryoSat – 2, J. Geophys. Res.-Oceans, 124, 7473–7485, https://doi.org/10.1029/2019JC015232, 2019.

Tivy, A., Howell, S. E. L., Alt, B., McCourt, S., Chagnon, R., Crocker, G., Carrieres, T., and Yackel, J. J.: Trends and variability in summer sea ice cover in the Canadian Arctic based on the Canadian Ice Service Digital Archive, 1960–2008 and 1968–2008, J. Geophys. Res.-Oceans, 116, C03007, https://doi.org/10.1029/2009JC005855, 2011.

Tschudi, M. A., Stroeve, J. C., and Stewart, J. S.: Relating the age of Arctic sea ice to its thickness, as measured during NASA's ICESat and IceBridge campaigns, Remote Sens., 8, 6, https://doi.org/10.3390/rs8060457, 2016.

Willatt, R., Laxon, S., Giles, K., Cullen, R., Haas, C., and Helm, V.: Ku-band radar penetration into snow cover on Arctic sea ice using airborne data, Ann. Glaciol., 52, 197–205, https://doi.org/10.3189/172756411795931589, 2011.

Zhang, J. and Rothrock, D.: Modeling global sea ice with a thickness and enthalpy distribution model in generalized curvilinear coordinates, Mon. Weather Rev., 131, 845–861, https://doi.org/10.1175/1520-0493(2003)131<0845:MGSIWA>2.0.CO;2, 2003.

Zhang, Z., Yu, Y., Li, X., Hui, F., Cheng, X., and Chen, Z.: Arctic sea ice classification using microwave scatterometer and radiometer data during 2002–2017, IEEE T. Geosci. Remote, 57, 5319–5328, https://doi.org/10.1109/TGRS.2019.2898872, 2019.